Machine learning reveals the control mechanics of the insect wing hinge.

Johan M. Melis and Michael H. Dickinson
Division of Biology and Bioengineering, California Institute of Technology, Pasadena CA 91125

Abstract

Insects constitute the most species-rich radiation of metazoa, a success due primarily to the evolution of active flight. Unlike pterosaurs, birds, and bats, the wings of insects did not evolve from legs[1], but are novel structures attached to the body via a biomechanically complex hinge that transforms the tiny, high-frequency oscillations of specialized power muscles into the sweeping back-and-forth motion of the wings[2]. Due to the minute size and morphological complexity, the basic mechanics of the hinge are poorly understood. The hinge consists of a series of tiny, hardened structures called sclerites that are interconnected to one another via flexible joints and regulated by the activity of a set of specialized steering muscles. In this study, we imaged the activity of these steering muscles in a fly using a genetically encoded calcium indicator, while simultaneously tracking the 3D motion of the wings with high-speed cameras. Using machine learning approaches, we created a convolutional neural network[3] that accurately predicts wing motion from the activity of the steering muscles, and an autoencoder[4] that predicts the mechanical role of the individual sclerites on wing motion. By replaying patterns of wing motion on a dynamically scaled robotic fly, we quantified the effects of steering muscle activity on the production of aerodynamic forces. A physics-based simulation that incorporates our model of the wing hinge generates flight maneuvers that are remarkably similar to those of free flying flies. This integrative, multi-disciplinary approach reveals the mechanical control logic of the insect wing hinge, arguably the most sophisticated and evolutionarily important skeletal structure in the natural world.

Whether to forage, migrate, reproduce, or avoid predators, aerial maneuverability is essential for flying insects. Most insects actuate their wings using two morphologically and functionally distinct sets of muscles. Contractions of the large, indirect flight muscles (IFMs) are activated mechanically by stretch rather than by individual action potentials in their motor neurons—a specialization that permits the production of elevated power at high wingbeat frequency[5,6]. There are two sets of IFMs, dorso-ventral muscles (DVMs) and the dorso-longitudinal muscles (DLMs), arranged orthogonally to maintain a self-sustaining oscillation (Fig. c-e). The tiny deformations in the exoskeleton generated by the IFMs are mechanically amplified by the wing hinge[7–11], an intricate structure consisting of an interconnected set of small sclerites embedded within more flexible exoskeleton and regulated by a set of small control muscles[12] (Fig. a,b). The mechanical operation of the hinge remains enigmatic, because the sclerites are difficult to visualize externally and move so rapidly that their motion during flight has not been accurately captured by either stroboscopic photography[13], high speed videography[14], or X-ray tomography[15].

The consensus of all prior morphological analyses[2,8,9,11,15] suggests that the tiny deformations of the thorax generated by contractions of the IFMs are transformed into wing motion via the mechanical actions of the anterior and posterior-medial notal wing processes (ANP and PMNP) on the 'x'-shaped 1st axillary sclerite (ax1) at the base of the wing (Fig. 1a,b). The ANP projects from the anterior end of the parascutal shelf and fits in the groove between the two anterior lobes of ax1. The PMNP sits at the anterior end of the large scutellar lever arm (SLA), in a notch between the two ventral lobes of ax1. Contractions of the DLMs during the downstroke are thought to be transmitted to the wing hinge via two main mechanisms: (1) a rotation of the scutellum along its junction with the notum that moves the scutellar lever arm and PMNP upward, and (2) an elevation of the entire notum that raises the ANP at the lateral edge of the parascutal shelf (Fig. 1d). Contractions of the antagonistic DVMs during the upstroke cause the opposite

effects (Fig. 1e). The more distal 2nd axillary sclerite (ax2) possesses a dorsal flange that fits between the two dorsal protuberances of ax1, coupling the two sclerites during flight. Ax2 is a critical component of the hinge system because it is rigidly attached to the radial vein—the main structural spar of the wing—and it has an anteriorly projecting ventral extension that fits into a notch in the plural wing process (PWP), thus forming the main fulcrum for wing motion (Fig. 1b,g). Because this fulcrum point is distal and anterior to ax1 (Fig. 1b), upward motion of the SLA causes downward motion and pronanation of the wing, whereas downward motion of the SLA causes upward motion and supination of the wing[7].

In addition to the SLA, the anterior end of the scutellum is connected to another anteriorly projecting structure, the 4th axillary sclerite (ax4), thus providing another system linking IFM strains to the wing base (Fig. 1d). Ax4 lies ventrolateral to the SLA and is attached by a previously unnamed sclerite (US) to the 3rd axillary sclerite (ax3), which itself contacts both ax1 and ax2, as well as the base of the anal vein, the main structural spar for the posterior half of the wing (Fig. 1b). Due to its connection with the anal vein, the linkage system consisting of the scutellum, ax4, US, and ax3 could influence wing camber and angle of attack during flight[9,16], but this functional role remains speculative. We note that some prior authors have drawn the US as an extension of ax3[16,17], but the two structures appear distinct in more recent μ-CT data[18].

In addition to the four axillary sclerites that are directly incorporated into the hinge, there is another important sclerite, the basalare, which sits in the membranous episternal cleft just anterior to the wing (Fig. 1f,g)[13,15,19]. From the surface, the basalare is a triangular-shaped structure, but it has a long internal invagination (apophysis) that provides an attachment site for two of its steering muscles (Fig. 1h). During flight, the basalare is thought to oscillate passively due to the opening and closing of the episternal cleft and via its ligamentous connection to the base the radial vein. However, the magnitude of these oscillations and the mean position of the basalare is actively regulated by its three control muscles[15,20], thereby adjusting the tension of the ligamentous connection to the radial vein.

Although the IFMs provide the power to oscillate the wings, they cannot regulate the rapid changes in kinematics required for flight maneuvers or the sustained asymmetrical patterns of motion required to remain aloft with damaged wings[21]. In flies, that control is mediated by a set of 12 steering muscles that insert on three of the four sclerites (ax1, ax3, ax4) and the basalare (Fig. 1f-h). The steering muscles are named after the sclerite on which they act (ax1: i1 and i2; ax3: iii1, iii2, iii3; ax4: iv1, iv2, iv3, and iv4; basalare: b1, b2, and b3). Ax4 and its muscles are sometimes described using an alternative nomenclature, hg, after its German name 'hinter-Gelenkforsatz'[17]. Each steering muscle is innervated by only a single excitatory motor neuron[22,23], so that the entire flight motor system is remarkably sparse relative to comparably maneuverable vertebrates such as hummingbirds[24].

To investigate the function of the wing hinge using a machine learning approach, we constructed an experimental apparatus that allowed us to image steering muscle activity and wing kinematics simultaneously (Fig. 2a). We captured the wing motion of tethered flies at 15,000 frames per second using three high-speed cameras, while simultaneously measuring steering muscle activity using the calcium indicator, GCaMP7f[25] (Extended Data Fig. 1). To capture data sequences that represented a wide range of muscle activity, we collected a large set of sequences, each triggered whenever the activity of one of the steering muscles (chosen *a priori* at the start of each trial) exceeded a user-defined threshold. To encourage a wide variety of flight behaviors, we also displayed a panel of open- and closed-loop visual stimuli on a cylindrical array of LEDs[26] surrounding the fly (Extended Data Fig. 1a,b). In total, we recorded a total of 479 flight sequences from 82 flies. After excluding a subset of wingbeats from sequences when the fly either stopped flying or flew at an abnormally low wingbeat frequency, we obtained a final dataset of 76,270 wingbeats.

To reconstruct the kinematics of the wings from the high-speed data, we developed an automated tracking algorithm that used a trained convolutional neural network (CNN)[27] and particle swarm optimization[28] (Extended Data Fig. 2a). We specified wing pose relative to a fixed reference frame that approximated the mean stroke plane using three Tait-Bryan angles: stroke position (ϕ), deviation (θ), and wing pitch (η) (Fig. 2b). We also defined a fourth angle (ξ) that quantified the chord-wise deformation of the wing (i.e. camber) from the leading to the trailing edge (Fig. 2c). We parsed the wing kinematic traces into separate wingbeats, beginning and ending at dorsal stroke reversal. To reduce the dimensionality of the data, we fitted Legendre polynomials to all four kinematic angles, creating a vector of 80 coefficients ($\phi = 16$, $\theta = 20$, $\eta = 24$, $\xi = 20$) that collectively captures the motion of one wing during each stroke with high accuracy.

We determined the Ca^{2+} signals originating from each of the 12 steering muscles using a real-time unmixing model as previously described[25]. The muscle activity traces were normalized over each trial duration, such that 0 and 1 corresponded to -2 and +2 standard deviations (σ), respectively (Fig. 3a). Due to its binding kinetics[29], GCaMP7f reports a low-pass filtered version of sarcoplasmic Ca^{2+} levels, which in addition to attenuating high frequencies, introduces a time delay between changes in ion concentration and fluorescence signals. Because of these effects, the muscle signals relevant for the kinematics of any individual stroke are spread out over many stroke cycles, and the GCaMP7f data recorded after a particular wingbeat are better representative of the Ca^{2+} levels in the muscles at the time the kinematic measurements were made. Thus, when training and evaluating our CNN, we associated the kinematics of each individual wingstroke with the Ca^{2+} signals recorded in the muscles the during the subsequent 9 strokes.

To determine if a machine learning algorithm could accurately predict wing motion solely from the activity of the steering muscles, we constructed a CNN consisting of two convolutional layers and two fully connected layers (Fig. 3b). We trained this network using 85% of our dataset, reserving the rest as a test set. For each wingbeat, the 13x9 matrix of muscle activity and wingbeat frequency provided the input to the network, whereas the output consisted of a vector containing the 80 Legendre coefficients encoding the four angles of wing motion. Despite the fact that the network was trained using a measure of muscle activity filtered by GCaMP7f kinetics, it nevertheless predicted the salient modulations in wing motion throughout the measured sequences with remarkable accuracy (Fig. 3c, Extended Data Figs. 3,4). The success of the trained network suggests that the activity of the 12 direct steering muscles provides sufficient information to accurately reconstruct the intricate pattern of wing motion.

A previous study found that steering muscles can be roughly categorized by their activity pattern into phasic muscles (e.g. b2, i1, iii1, iv1) that fire sporadically in bursts, and tonic muscles (e.g. b1, b3, i2, iii3, iv4) that exhibit more continuous patterns of activity[25]. We observed roughly the same pattern in our more limited dataset (Fig. 4a). To quantify the degree to which the activities of different steering muscles were linked, we performed a correlation analysis on the muscle activity, and found several strong linear trends among muscles (Extended Data Fig. 5). We used random sample consensus (RANSAC)[30] to fit a linear models to the correlations in the dataset, and assumed that all possible patterns of muscle activity reside within the resulting 12-dimensional plane. We did not find any significant correlation between streering muscle activity and wingbeat frequency.

We next used our CNN model of the hinge to investigate the transformation between muscle activity and wing motion by performing a set of virtual manipulations, effectively using the network to execute experiments that would be difficult, if not impossible, to perform on actual flies. As a starting point, we defined a baseline pattern of muscle activity that was derived from sequences without any noticeable changes in muscle fluorescence and wing motion (grey data, Fig. 4b,c). From this starting point, we could

then manipulate the network inputs to systematically increase the activity of each individual steering muscle, along with proportional changes in the activity of the other muscles with which it is correlated (colored data, Fig. 4b,c). The kinematic consequences of increasing the relative activity of each steering muscle to 1, representing maximal activity, are plotted in the columns of Fig. 4c. From these data, it is possible to identify the correlations between muscle activation and changes in wing motion, as one might do in an actual physiology experiment in which the activity of each steering muscle was recorded in isolation. The results of these virtual experiments are consistent with prior experimental data from the subset of steering muscles for which electrophysiological recordings have been possible. For example, activation of the b1 and b2 muscles is known to correlate with an increase in stroke amplitude and deviation[20,31]. Although electrophysiological recordings from b3 have not been feasible due to its small size, the antagonistic effects relative to b1 are consistent with the morphological arrangement of these two muscles. Similarly, the activity of i1 is known to correlate with a decrease in stroke amplitude and deviation, whereas the activity of the muscles of ax3 are correlated with increases in these parameters[31,32]. The consistency of our model's predictions with these prior observations provides confidence that the CNN converged on a solution that captures the salient features of wing hinge mechanics.

Collectively, the results of the virtual experiments conducted using our CCN hinge model indicate that the 12 steering muscles act in a coordinated manner to regulate subtle changes in wing motion. To examine the aerodynamic consequences of these changes, we used a dynamically scaled flapping robot[33] to measure how flight forces would change with alterations in the activity of each muscle (Extended Data Fig. 6). The motion of the leading edge of the robotic wing was controlled by a system of servo motors that specified the three wing angles (ϕ, θ, and η). Unlike earlier versions, which modeled the wing as a solid flat planform[34], our new robotic wing consisted of 4 span-wise wedges connected by three hinge lines approximating the positions of wing veins L3, L4, and L5 (Fig. 1a, 2c, Extended Data Fig. 6a). We could actuate the angles at each hinge line via servo motors attached to the base of the wing, thus specifying the fourth kinematic angle, ξ, which determines camber. A sensor at the base of the wing measured the aerodynamic forces and torques generated by the flapping motion of each kinematic pattern. We used the Newton-Euler equations to compute the inertial forces generated by the flapping wing, based on previously measured values of wing mass[35] and added them to the measured aerodynamic forces, thus obtaining a time history of forces and torques generated by the wing for each wingbeat (Extended Data Fig. 6c,d). We then conducted this analysis for the 12 kinematic patterns predicted by our CNN for the maximum activity of each steering muscle (Fig. 4), creating a map linking muscle activity to flight forces (Extended Data Fig. 7).

Using our aerodynamic data, we could then test whether our CNN linking muscle activity to wing motion could generate free flight maneuvers that resemble those executed by real flies. To do so, we used Model Predictive Control (MPC)[36] to determine the activity patterns within the array of 24 steering muscles (12 for each side) that generate any arbitrary flight maneuver in the shortest amount of time within a specified number of wingbeats (Fig. 5, Extended Data Fig. 8). The state vector of the system, x, consisted of 13 parameters that collectively specify the linear and angular velocity of the body in the strokeplane reference frame and the body quaternion and position in an inertial reference frame. The control vector, u, consisted of 24 parameters representing the left and right muscle activities. Our model also incorporated body drag, the inertial and aerodynamic damping of the wings[37], and gravitational forces. In Fig. 5a-b, we show a MPC simulation of a stereotypical free flight maneuver—a body saccade[38]—in which a fly rapidly changes direction in ~100 ms[39,40]. The MPC simulation starts in forward flight mode (0.3 m/s) and has to reach a goal state with a yaw rotation of 90° to the right within 10 wingbeats. Left and right steering muscle activity show relatively subtle changes during the maneuver, with the largest asymmetries in b1 and b3 activity (Fig. 5c). The saccade is achieved by a combination of roll, pitch and yaw rotations

with only a slight deceleration in forward velocity (Fig. 5d). Using the time course of muscle activity, we could reconstruct the left and right wing motion patterns during the saccade using our CNN model (Fig. 5e). The asymmetries in wing motion are subtle, corresponding remarkably well to those recorded during the free flight saccades of real flies[39,40]. We provide example MPC simulations of two other flight maneuvers (forward and backward acceleration) in Extended Data Fig. 8. It is noteworthy that even though our CCN network of the wing hinge was trained using muscle activity data that was filtered by the time constant of CGaMP7f binding, the model fly could nevertheless accomplish rapid maneuvers that closely resemble those of real flies.

In the simulated experiments summarized in Fig. 4, we deliberately incorporated the correlation patterns among muscles (Extended Data Fig. 5), so that the results could be most accurately compared to prior work and were similar to the conditions under which we trained the network. However, the strong correlations among muscles makes it difficult to isolate their individual effects on wing motion. To gain more insight into the mechanical function of the individual wing sclerites, we constructed and trained an autoencoder[4], with a network architecture that deliberately partitions the input data from the steering muscles into four nodes according to the sclerites on which they act, with an additional node assigned to wingbeat frequency (Extended Data Fig. 9). This narrow bottleneck of nodes forces the network to project muscle activity into a 5-dimensional latent-variable space, effectively performing a non-linear Principal Component Analysis[4]. A subsequent layer of the network correlates each of these latent variables to independent changes in wing motion. After training this modified network on the dataset, we could then predict the changes in wing motion resulting from the activity of the muscle groups associated with the four wing sclerites (Fig. 6).

Our analysis suggest that tension exerted on each sclerite modulates distinct aspects of wing motion (Fig. 6). For example, the b1 and b2 muscles act agonistically to increase stroke deviation and stroke amplitude during the downstroke, as well as advancing the phase of wing rotation at the start of the upstroke. The increased tension on the ligament connecting the basalare to the radial vein caused by contraction of b1 and b2 could explain these results (Fig. 6b), with the b3 muscle having an antagonistic effect. Increased downward tension on the 1st axillary caused by the activation i1 and i2 decreases stroke amplitude and reduces stroke deviation at the start of the upstroke (Fig. 6d). It is noteworthy that activation of iii2 and iii3 has almost precisely the opposite effect on wing motion as those caused by activation of ax1 muscles (Fig. 6e). The positions of the ax1 and ax3 muscle insertions relative to ax2 may provide a simple explanation for these antagonistic influences on wing motion. Although the ax2 has no control muscles, this critical sclerite forms the fulcrum upon which the wing oscillates via its joint with the PWP. Whereas the muscle insertions on ax1 sits medial to this fulcrum (Fig. 6d), those on ax3 reside distally[2,8,9,41] (Fig. 6e). Thus, whereas downward tension created by the i1 and i2 would tend to bias the mean stroke position of the wing upward (by pulling inboard of the fulcrum), tension created by the muscles of iii2 and iii3 would bias the wing downward (by pulling outboard of the fulcrum). The large iii1 muscle is rarely active during flight[25] and is likely homologous with the ancestral retractor muscle that is used for folding the wing along the body axis[41]. When the wing is extended during the flight, however, the tendons to which the iii2 and iii3 deflect around the PWP so that the muscles exert downward tension on ax3[9].

Our latent-variable analysis suggests that the ax4 muscles have a quite profound influence on wing motion (Fig 6b,f). Consistent with our virtual activation experiments using the fully connected CNN model (Fig. 4), increased activity of iv1 and iv2 decreases the magnitude of stroke amplitude, stroke deviation, and angle-of-attack throughout the entire wingbeat—changes that are antagonized by the activity of iv3 and iv4. A functional stratification of the ax4 muscles into two antagonistic groups has not been noted in previous physiological studies, although these muscles have proven particularly difficult to record due to their small size and tight clustering. However, prior morphological investigations have noted that the two muscle

groups insert via separate tendons that would cause different defections of ax4 that in turn could influence wing motion via the sclerite's connection to ax3[9,42]. We hypothesize that the action of the iv1 and iv2 muscles on the ax4 causes an inward movement of that sclerite that depresses the anal vein of the wing during the downstroke via its linkage to ax3, thereby greatly increasing the angle-of-attack (Fig. 6f) and reducing the lift-to-drag ratio. The increase in drag would further reduce lift by lowering wing velocity, which could explain the prominent drop in the stroke plane that our latent variable model predicts during an increase in iv1 and iv2 activity, with iv3 and iv4 activity having the opposite effect. This hypothesis requires that the wings possess a passive flexion joint, such that the distal wing blade responds to aerodynamic and inertial forces and not just to the mechanical drive imposed by the hinge. Evidence for just such a flexure line has been proposed for other fly species[43] and is evident in high speed imaging data collected during free flight in *Drosophila*, which clearly show that the wing blade extends beyond the maximum angular limit of the wing base during stroke reversal, with the deformation concentrated along a narrow line (Extended Data Fig. 10a). We have also found evidence for a cord-wise flexure line in *Drosophila* based on autofluorescence consistent with the present of resilin (Extended Data Fig. 10b). The existence of this flexion joint provides a passive mechanism that could explain how alterations in the in angle of attack caused by activity of the ax4 muscles could generate large changes in both stroke position and deviation throughout the wingstroke, and might also play a role permitting the storage and recovery of inertial energy via elastic storage[23,44,45] (Extended Data Fig. 10c-d).

In this study, we used machine learning to construct both a fully connected CNN model and an autoencoder of the fly's wing hinge based on the simultaneous measurement of steering muscle activity and wing kinematics. There are several reasons suggesting that our CNN model provides an accurate representation of the biomechanical processes that transform steering muscle activity to wing motion. First, when we used the network to predict the pattern of wing motion generated by the maximal activity of each muscle, the model's output was consistent with all prior experiments for which the pattern of muscle activity has been measured directly with electrodes (Fig. 4). Second, when we embedded the CNN hinge model into a state-space simulation of a flying fly and used MPC to determine the pattern of muscle activity that generated an array of different canonical flight maneuvers, the results in each case resemble the known behavior of freely flying flies (Fig. 5). Third, when we constructed an autoencoder in which the steering muscle activity was parsed into nodes representing the muscle groups inserting on each of the four wing sclerites (Fig. 6), the model's predictions were consistent with known features of hinge morphology and differences in the insertion patterns of control muscles. Collectively, our results generate a suite of specific hypotheses (Fig. 6c-f) that can be tested via a combination of additional experiments and a detailed, physics-based model of the hinge. Further, with the recent availability of a connectome for the VNC of *Drosophila*[44,45], we expect that these results will help provide a deeper understanding of flight control circuitry that underlies the recruitment of steering muscles during flight maneuvers.

Until recently, the morphologically complex wing hinge of flies and other neopterous insects was considered a derived trait that allows the wing to fold along the body axis when not in use, and for wing motion to be driven by the contraction of indirect flight muscles that do not insert at the base of the wing. The hinge found in extant paleopterous insects (dragonflies, damselflies, and mayflies), which is actuated by direct flight muscles and does not permit folding, was considered representative of the ancestral condition[46]. However, a new phylogeny derived from a comprehensive genetic analysis of the Polyneoptera provides a compelling reinterpretation[47], in which the unfoldable wing of the paleopterous orders is more parsimoniously interpreted as a radical simplification of the ancestral condition. According to this hypothesis, many features of the odonates—including the inability to fold their wings—are secondary specializations of their large size, perching habit, and predatory lifestyle[48–50]. Thus, despite the fact that *Drosophila* is a crown taxon, the analysis of its wing hinge could provide general insight into biomechanical innovations underling the evolution of insect flight.

Acknowledgements
The authors wish to thank several individuals whose efforts contributed to the work presented in this paper. Thad Lindsay assisted in the design of the epifluorescent microscope and data acquisition software used for muscle imaging. Will Dickson provided expertise in instrumentation, programming, and data analysis. Ainul Huda assisted in the construction of genetic lines required for the experiments. Jaison Omoto made the confocal images of wing autofluorescence. John Tuthill and Tony Azevedo offered a tomographic dataset of the *Drosophila* wing hinge that was collected at the European Synchrotron Radiation Facility in Grenoble, France. Sam Whitehead analyzed this tomography data to provide a preliminary reconstruction of the hinge sclerites, and offered critical feedback on the manuscript text and data presentation. Benjamin Fabian and Rolf Georg Beutel provided micro-CT data from their publication on the morphology of the adult fly body. Igor Siwanowiczi (Janelia Research Campus) generously shared preliminary data from his comprehensive morphological analysis of the *Drosophila* thorax, which was helpful for editing our drawings of wing hinge morphology. The research reported in this publication was supported by the National Institute of Neurological Disorders and Stroke of the NIH (U19NS104655).

Methods

Flies

We generated flies expressing GCaMP7f in steering muscles by crossing w[1118];+;P{y[+t7.7] w[+mC]=R22H05-Gal4}attP2 with +[HCS]; P{20XUAS-IVS-GCaMP7f}attP40;+. All experiments were conducted on the 3-day old female offspring of this cross. We anesthetized flies on 4°C cold plate to immobilize them and remove the anterior two pairs of legs at the coxa. The flies were then attached to a tungsten wire at the notum using UV-curing glue (Bondic). After a 10-minute recovery period, the tethered flies were placed into our experimental setup (Fig. 2a, Extended Data Fig. 1a,b).

High-speed camera recordings

We used three synchronized high-speed cameras (SA5, Photron) to image the fly from three different angles. The cameras recorded continuously at a rate of 15,000 frames per second (fps) with a shutter time of 1/30,000 seconds. To ensure sharp images of the fly under relatively low light conditions, we utilized telecentric lenses (0.5X PlatinumTL, Edmund Optics) and collimated infrared (850nm) backlights (M850LP1 LED and SM2P collimation lens, Thor Labs). The 3D calibration of the high-speed cameras was achieved using the Direct Linear Transformation (DLT) method[51], employing an IR-translucent acrylic cube with engraved circles at known 3D positions. We developed a custom Matlab (MathWorks) script for this calibration process. The recorded images had a resolution of 256x256 pixels with an 8-bit intensity depth. To optimize data storage, we divided the camera memory buffers into 8 partitions. Each partition could accommodate 8 sequences, each lasting 1.1 seconds and containing 16,376 frames. The cameras were set to save a sequence centered around the trigger event from all three cameras into the respective partition. Once all partitions were full, the videos were transferred in raw format to a hard drive.

Real-time calcium imaging

We employed a previously described technique[25] to visualize muscle activity using GCaMP7f in the fly by utilizing single photon excitation through the cuticle. A blue LED (M470L3, Thor Labs) served as the excitation light source, which was directed through a 480/40 nm excitation filter (Chroma) and focused onto the fly using a 4x lens (CFI Plan Fluor, Nikon). The resulting fluorescent light passed through a 535/50 nm emission filter (Chroma) and was captured by a machine vision camera (BF3-U3-04S2M-CS, FLIR). To synchronize the imaging process, we utilized an optoelectronic wingbeat analyzer[52] to strobe the blue excitation LED for 1 ms at the dorsal stroke reversal of each wingbeat. The fluorescence camera was strobed at half the wingbeat frequency (~100 fps), resulting in each frame containing two consecutive illuminations of the thorax. To synchronize the high-speed and fluorescence image streams, we employed a microcontroller (Teensy 3.2) that received synchronization pulses from the high-speed cameras and counted them. Additionally, the microcontroller received the ventral stroke reversal signal from the wingbeat analyzer and coordinated the strobe signals to the blue excitation LED and the machine vision camera. The fluorescence images, along with a high-speed pulse count serving as a timestamp, were saved using a combination of the Robotic Operating System (ROS, www.ros.org) and custom-written Python scripts.

Muscle activity unmixing and triggering

Fluorescence images were received by a computer running ROS at half the wingbeat frequency during flight or at 100 fps when the fly was not flying. Each acquired fluorescence image was indexed by attaching the current timestamp from the Teensy 3.2 ROS node. An unmixing algorithm, described elsewhere[25], was applied to extract the Ca^{2+} signal from the overlapping muscles. To initialize an experiment, a set of ROIs in a GUI was used to orient and scale the 3D muscle model to the image using an affine transformation. The resulting fluorescence image and data vector capturing the activity of all 12 steering muscles were

saved in an hdf5 file. The muscle activity vector was stored in a rolling buffer within ROS, covering approximately 30 seconds of data.

Our objective was to trigger the high-speed cameras based on rapid changes in muscle activity. To achieve this, a separate ROS node monitored the activity of a predefined muscle of interest throughout the experiment. At the start of each trial, we selected a muscle and an activity threshold for the trigger level. During the experiment, the trigger node calculated the gradient of the trigger muscle activity over 3 frames (equivalent to 6 wingbeats) and normalized this signal by dividing it by the standard deviation over a 30-second rolling buffer. Whenever the absolute value of the gradient exceeded the activity threshold, indicating a significant increase or decrease in muscle activity, the high-speed cameras were triggered. A 30-second refractory period after each trigger event ensured there was no overlap between subsequent high-speed sequences. The ROS system kept track of the number of triggers, and once 8 triggers were reached, the hdf5 file was closed and the high-speed cameras began transferring the sequences to a hard drive. In total, we recorded data from 82 flies, resulting in 479 high-speed videos (Extended Data Table 1). We aimed to record sequences triggered on all 12 muscles from a minimum of 5 flies each. However, the iii1 muscle exhibited sporadic activity, primarily during flight starts and stops, whereas iii2 displayed more gradual changes in activity compared to other muscles. As a result, we were only able to capture data from 4 flies for iii1 and iii2.

Automated wing pose reconstruction

We developed *FlyNet*, an automated tracking algorithm to extract body and wing pose. FlyNet consists of two steps: (1) a Convolutional Neural Network (CNN) predicts pose vectors of body and wing components based on a triplet of synchronous high-speed images, and (2) Particle Swarm Optimization (PSO) refines the CNN prediction using 3D model fitting. A GUI was created to load images, scale the 3D fly model, annotate images, and run the automated tracking algorithm. The 3D fly model includes the head, thorax, abdomen, left wing, and right wing, each with a pose vector comprising a quaternion, q, and position, p. For the wing pose an additional parameter, ξ, was used to capture wing deformation. The CNN, built using Tensorflow (www.tensorflow.ord) and Keras (keras.io) in Python 3, consists of a convolutional block to extract image features in each camera view, followed by a fully connected layer of 1024 neurons with SELU activation functions[53] and a final layer of 37 neurons (linear activations) corresponding to the pose vectors of the five 3D model components (Extended Data Fig. 2a). The CNN was trained on a dataset of more than 2000 frame triplets and model pose vectors. Each frame triplet was labelled by positioning, orienting and scaling the 3D model in the FlyNet GUI, such that the model projection onto the three camera views showed maximum overlap. After training the CNN for 100 epochs with mean squared error (mse) loss, the CNN pose predictions were close to the actual pose. However, to obtain the required accuracy, the PSO refinement step was crucial. The refinement began by segmenting images into background, wing, and body pixels. Body segments were obtained using an intensity threshold, while background and wing segments were separated using the minimum intensity image from image batches (100 frames per batch). The PSO refinement involved placing 16 particles at randomized initial positions around the predicted pose vector for each model component. Similarly, each particle starts with a randomized initial velocity. Over a fixed number of iterations (300), particles moved through parameter space according to the following update rules for position and velocity:

$$x^{k+1} = x^k + v^{k+1} \text{ , and} \tag{1}$$
$$v^{k+1} = w \cdot v^k + c_1 \cdot r_1 \cdot \left(p_{best} - x^k\right) + c_2 \cdot r_2 \cdot \left(g_{best} - x^k\right) , \tag{2}$$

where k is the iteration number, x is the parameter vector, v the velocity vector, w the momentum, c_1 and c_2 are constants, r_1 and r_2 are two random sample vectors from a normal distribution, p_{best} (personal

best) is the best scoring parameter vector of the particle, and g_{best} (global best) is the best scoring parameter vector of all particles. The constants w, c_1 and c_2 were set to 0.5, 0.3 and 0.3, respectively. At each iteration, the algorithm evaluates the cost function for each particle and determines whether the its personal and global best vectors need to be updated. The cost function is:

$$C_j = \sum_{n=1}^{3} \frac{I_n^b \Delta I_{n,j}^p}{I_n^b \cup I_{n,j}^{pj}}, \tag{3}$$

where C_j is the cost scalar for the 3D model component j, I_n^b is the binary image for camera view n, I_n^p is the back-projected binary image of the 3D model component j in camera view n, Δ is the symmetric image difference and $\cup$ is the image union. We implemented the PSO algorithm in C++ using the Standard Template Library (STL) in combination with the Threading Building Blocks library (TBB) to allow for multithreading on all CPU cores. The symmetric difference and union computations were performed as bitwise operations using dynamic bitsets in the Boost library. We achieved additional efficiency by running the PSO on the 3D model components independently, which reduced both the number of particles and iterations required for convergence. PSO is a global optimization method and convergence is not guaranteed. After 300 iterations, we found that the optimization had converged to either the global minimum predicted from human annotation or an obvious local minimum (for example the leading edge and trailing edge of the wing were flipped). Using a 32 CPU core computer with a Nvidia 1080 GPU, the algorithm took ~80 ms per frame triplet to predict and refine the pose vectors of all model components. For this study, we reconstructed body and wing pose vectors from a total of 7.8 million frame triplets.

Kalman filtering

Following the tracking process with FlyNet, we applied an Extended Kalman Filter (EKF)[54] to achieve temporal smoothing of body and wing pose. Each model component's pose vector was independently filtered, incorporating the first and second order temporal derivatives to ensure smooth motion. The system matrix utilized the temporal derivative of quaternions and a Maclaurin series of position and wing deformation. The measurement matrix, based on the tracking results, was a simple identity matrix. To achieve optimal smoothing, we performed a forward pass of the EKF, which resulted in smoothed traces but with a slight phase advance. To address this, we implemented a backward pass using a Rauch-Tung-Striebel smoother, which not only eliminated the phase advance but also provided additional smoothing. The FlyNet GUI enabled users to adjust the system covariance, allowing control over the degree of filtering for each pose parameter.

Strokeplane reference frame and wing kinematic angles

To establish the alignment of the Strokeplane Reference Frame (SRF) with the inertial reference frame, we conducted a Principal Component Analysis on the left and right wing root traces. This analysis determined the y, x, and z axes of the SRF, which corresponded to the first, second, and third principal components of the root traces, respectively. Once the SRF was defined, we used three Tait-Bryan angles to specify the orientation of the leading edge of the wing: stroke angle φ, deviation angle θ, and wing pitch angle η. Additionally, we introduced a fourth angle, ξ, to describe wing deformation along three flexure lines associated with the L3, L4, and L5 wing veins (Fig. 1a). We assumed equal division of the total deformation angle among these three spanwise flexure lines (Extended Data Fig. 2b).

Wingbeat parsing and Legendre polynomial fitting

We divided the wing kinematic angle traces into individual wingbeats starting and ending with dorsal stroke reversal. To facilitate comparison between wingbeats of different durations, we normalized the

wingbeat period to 1 and computed the wingbeat frequency, f, for each wingbeat. To accurately quantify the complex time history of wing motion, we fit Legendre polynomials to the 4 wing kinematic angles for each wingbeat. The Legendre polynomials are described by the Rodrigues' formula:

$$P_n(x) = \frac{1}{2^n n!}\frac{d^n}{dx^n}(x^2-1)^n, \tag{4}$$

where $P_n(x)$ is a Legendre polynomial of degree n, x the interpolation points over the interval $[-1,1]$, and d^n/dx^n the nth derivative of x. We fit a Legendre polynomial basis of degree n to each wing kinematic angle using a restricted least-squares fit. An ordinary least-squares solution, β, uses the Legendre polynomial basis, X, and the tracked data points, y, to find the Legendre coefficients that match the trace most accurately:

$$\beta = (X^T X)^{-1} X^T y. \tag{5}$$

A restricted least-squares fit[55], β^*, makes use of an ordinary least-squares solution, a restriction matrix, R, and a restriction vector, r, to incorporate the constraints:

$$\beta^* = \beta - (X^T X)^{-1} R^T (R(X^T X)^{-1} R^T)^{-1} (R\beta - r). \tag{6}$$

The constraints on the least-squares fit ensure that the wing kinematic traces are continuous up to the fourth temporal derivative between wingbeat transitions. For each wing kinematic angle, we tried a varying number of polynomials for the restricted least-squares fitting such that rapid rotations were captured by the fit but there was no overfitting. The Runge's phenomenon[56] introduces artificial oscillations at the edges of the fitting result when a large number of polynomials are used. Restricted least-squares fitting suppresses Runge's phenomenon and we found that a fit with up to 24 polynomials can accurately capture the kinetics without overfitting ($n_\phi = 16, n_\theta = 20, n_\eta = 24, n_\xi = 20$).

Outlier rejection, normalization, and training of the CNN

From the initial dataset of 83,056 wingbeats obtained through wingbeat parsing and Legendre polynomial fitting, we removed unrealistic flight conditions by excluding wingbeats with frequencies outside the range of 150 to 250 Hz and outliers exceeding the specified angle limits for each wing kinematic angle ($[-120° \leq \phi \leq 120°]$, $[-60° \leq \theta \leq 60°]$, $[-150° \leq \eta \leq 150°]$, $[-90° \leq \xi \leq 90°]$). These two criteria eliminated 8.2% of the data, resulting in a final dataset of 76,270 wingbeats. Prior to training the CNN, we normalized the muscle activity dataset by dividing the GCaMP7f traces by their respective standard deviations over the entire experiment duration. We also normalized the wingbeat frequency by mapping 150 Hz to 0 and 250 Hz to 1. These normalized values formed the input data for the CNN, consisting of a 13x9 matrix representing 12 muscle activity values and wingbeat frequency over 9 wingbeats. The output data comprised the 80 normalized Legendre coefficients for the left wing kinematic angles, the coefficients were normalized by dividing by π to range between -1 and 1. The CNN employed a sliding window of 9 wingbeats as input and predicted the Legendre coefficients for the first wingbeat of the window. To match the muscle fluorescence recorded at half the wingbeat frequency, we interpolated the muscle fluorescence at each wingbeat. We allocated the first 30 wingbeats from each high-speed video sequence for validation, while the remaining wingbeats were used for training. The training and validation datasets, consisting of 61,351 and 10,868 wingbeats respectively, were randomly shuffled. The CNN was trained for 1000 epochs using a batch size of 100, a learning rate of 10^{-4}, and a learning rate decay of 10^{-7} per epoch. The mse served as the loss function. Gaussian noise with a standard deviation of 0.05

was added to the network input to enhance noise robustness. After shuffling the dataset following each epoch, the training and validation losses reached mse values of $10^{-3.33}$ and $10^{-3.07}$, respectively.

To evaluate the accuracy of the learned mapping between muscle activity and wing motion, the trained CNN was used to predict wing motion for each validation sequence based on the muscle activity data. The predicted coefficient vector was multiplied by π and separated into coefficients for the four wing kinematic angles. Multiplication of the Legendre coefficient vectors by the Legendre polynomial bases, allowed the recovery of the four wing kinematic angles during a wingbeat. Extended Data Figs. 3 and 4 illustrate examples of different sequences showing muscle activity, wingbeat frequency, predicted wing motion, and tracked wing motion.

Muscle activity correlation analysis

We conducted a linear correlation analysis on the muscle activity in our dataset. For each steering muscle, we selected samples with an average gradient larger than 0.005 over the 9-wingbeat window of muscle fluorescence. This criterion was based on the sharp rise and slow decay of the GCaMP7f fluorescence kernel in response to muscle activation. Scatterplots illustrating the correlations between steering muscle fluorescence and wingbeat frequency for the gradient-selected wingbeats are presented in External Data Fig. 5. By employing linear models with RANSAC fitting, we determined the slopes and intercepts for all muscle correlations. Excluding the wingbeat frequency, muscle activity can be assumed to reside on a 12-dimensional plane. To ensure that all linear correlations in muscle activity share a common origin, we defined a baseline muscle activity pattern. This involved identifying sequences in the dataset with no significant changes in muscle activity or wing motion and setting the wingbeat frequency to 200 Hz. In Extended Data Fig. 5, the intercepts of the linear model were adjusted such that the baseline muscle activity pattern aligns with the 12-dimensional plane (Extended Data Table 2).

Virtual experiments

To conduct virtual experiments on the wing hinge (Fig. 4), we utilized the linear model provided in Extended Data Table 2 in conjunction with the trained CNN. In order to obtain realistic inputs to the CNN, we used the linear model to find steering muscle activity patterns that are within the manifold of the dataset that was used to train the CNN. The process began by determining the baseline wing kinematics through the CNN's prediction of the wing motion corresponding to the baseline muscle activity pattern. Becuase the CNN requires 9 wingbeats of muscle activity as input, the baseline muscle activity pattern was repeated 9 times. To find the maximum muscle activity patterns for each muscle, we traversed the 12-dimensional surface from the baseline muscle activity pattern to a point where the specific muscle reached an activity value of 1.

RoboFly experiments

The aerodynamic forces generated by the baseline and maximum muscle activity patterns predicted by the CNN were assessed using a dynamically-scaled robotic wing (RoboFly). RoboFly contained a stepper motor (IMS M-2231-3) controlling ϕ through two gears with a 1:3 ratio, as well as two servo motors (HiTec D951TW) controlling θ and η. A 6-degree-of-freedom sensor (ATI Nano 17) captured forces and torques along three orthogonal axes at the wing's base. A microcontroller (Teensy 3.2), operating at 100 Hz, updated stepper and servo positions and collected sensor data (Extended Data Fig. 6a). The wing itself consisted of four acrylic panels and three micro-servos (HiTec HS-7115TH) at the base, collectively controlling the fourth wing kinematic angle, ξ. Each trial involved repeating the programmed motion pattern for seven wingbeats. The commands for the first and last wingbeats of each sequence were multiplied by the first and second quarter, respectively, of a $\sin^2(t/T)$ function, ensuring that the wing began and ended at the home position ($\phi, \theta, \eta, \xi = 0$). To reach steady-state conditions for wake effects,

the measurements from the first three wingbeats were discarded[57], and we calculated median force and torque values over wingbeats 4, 5, and 6. In a separate experiment, gravitational and buoyancy forces acting on the wing were measured by playing back the wing motion at a 1/5 reduced speed, enabling subtraction of the gravity measurement from the corresponding 1X speed experiment to isolate aerodynamic forces and torques.

Inertial forces and torques

To calculate the inertial forces acting on the wing, we applied the Newton-Euler equations (Extended Data Fig 6b). These equations consist of two components: forces and torques due to acceleration (F_{acc}, T_{acc}) and velocity (F_{vel}, T_{vel}). The inertia tensor of the wing was determined using the scaled 3D model of the wing and an estimated wing mass of $m_{wing} = 1.6 \cdot 10^{-9}$ kg[35]. Consistent with previous experiments, the inertial forces and torques were found to be of similar magnitude as the aerodynamic forces[58] (Extended Data Fig 6c). The total forces and torques resulting from wing motion were obtained by summing the individual components:

$$F_{total} = F_{aero} + F_{acc} + F_{vel}, \text{ and} \tag{7}$$
$$T_{total} = T_{aero} + T_{acc} + T_{vel}. \tag{8}$$

State-space system of fly flight

To model fly flight incorporating our CNN results and aerodynamic measurements, we developed a state-space model. The system's state vector consists of the velocity (v), angular velocity (ω), quaternion (q), and position (p) of the fly's body. By differentiating the state vector, we obtained the temporal derivative ($\dot{x}$), which includes acceleration (a), angular acceleration ($\dot{\omega}$), velocity (v), and angular velocity (ω). All state parameters are in the body's reference frame, except for the body quaternion and position, which describe the orientation and position relative to an inertial reference frame. Using the Newton-Euler equations and positioning the reference frame at the body's center of gravity, we derived the body inertia tensor:

$$M_{body} = \begin{bmatrix} m_{body} & 0 \\ 0 & I_{body} \end{bmatrix}. \tag{9}$$

The body mass (m_{body}) and inertia matrix (I_{body}) were estimated using scaled 3D models of the head, thorax and abdomen, and an assumed body density of $1200\ \mathrm{kg/m^3}$ (Extended Data Table 3). With the SRF positioned at the center of gravity, the equation of motion for the body becomes:

$$\begin{bmatrix} F \\ T \end{bmatrix} = M_{body} \begin{bmatrix} a \\ \dot{\omega} \end{bmatrix}. \tag{10}$$

In free flight, the body of the fly experiences aerodynamic drag, gravitational forces and the forces generated by wing motion. We estimate the body drag, F_D, by assuming that the body corresponds to a sphere with a $1\ \mathrm{mm}$ radius and a drag coefficient of 0.5:

$$F_D = 0.5\pi \cdot sign(v) \cdot v^2, \tag{11}$$

where $sign(v)$ computes the sign of the body velocity along each cardinal axis. The gravitational force on the body can be computed using:

$$F_G = m_{body} \cdot g \cdot \begin{bmatrix} 2(q_x q_z - q_y q_0) \\ 2(q_y q_z + q_x q_0) \\ 1 - 2(q_x^2 + q_y^2) \end{bmatrix}, \tag{12}$$

where $g = 9800\ \mathrm{mm/s^2}$ is the gravitational acceleration and q the body quaternion. During rapid body translation and rotation, aerodynamic and inertial damping[37,59] usually counteract the motion. We computed the aerodynamic ($\partial F_A/\partial v,\ \partial T_A/\partial v,\ \partial F_A/\partial \omega,\ \partial T_A/\partial \omega$) and inertial ($\partial F_I/\partial \omega,\ \partial T_I/\partial \omega$) damping coefficients using the quasi-steady aerodynamic model[60,61] and the Newton-Euler equations for the baseline wing kinematics. The RoboFly experiments in combination with the inertial force computations yield the control forces and torques for a fly in hovering flight. By subtracting the forces and torques produced by the baseline wing kinematics from the forces and torques measured for the maximum muscle activity wingbeats, and subsequently dividing by the difference between maximum muscle activity (=1) and the baseline muscle activity value of the specific muscle, we obtain the Jacobian for control forces and torques ($\partial F_C/\partial u,\ \partial T_C/\partial u$). The RoboFly measurements and steering muscle fluorescence recordings were both performed on the left wing: the right control Jacobian was obtained by mirroring the left control Jacobian (Extended Data Table 3). When we insert all the forces and torques acting on the body, we get the following equations of motion:

$$\begin{bmatrix} F_G + F_D \\ 0 \end{bmatrix} + \begin{bmatrix} F_{base} \\ T_{base} \end{bmatrix} + \begin{bmatrix} \partial F_A/\partial v & \partial F_A/\partial \omega \\ \partial T_A/\partial v & \partial T_A/\partial \omega \end{bmatrix} \begin{bmatrix} v \\ \omega \end{bmatrix} + \begin{bmatrix} \partial F_I/\partial \omega \\ \partial F_I/\partial \omega \end{bmatrix} \omega + \begin{bmatrix} \partial F_T/\partial u_L \\ \partial T_T/\partial u_L \end{bmatrix} u_L + \begin{bmatrix} \partial F_T/\partial u_R \\ \partial T_T/\partial u_R \end{bmatrix} u_R = M_{body} \begin{bmatrix} a \\ \dot{\omega} \end{bmatrix}, \tag{13}$$

where u_L and u_R represent the left and right steering muscle activity respectively (baseline muscle activity subtracted), and F_{base} and T_{base} correspond to the baseline wing kinematics forces and torques. We can split the equations of motion into a system matrix ($A(x)$) and control matrix ($B(u_L, u_R)$):

$$A(x) = M_{body}^{-1} \left(\begin{bmatrix} F_G + F_D \\ 0 \end{bmatrix} + \begin{bmatrix} F_{base} \\ T_{base} \end{bmatrix} + \begin{bmatrix} \partial F_A/\partial v & \partial F_A/\partial \omega \\ \partial T_A/\partial v & \partial T_A/\partial \omega \end{bmatrix} \begin{bmatrix} v \\ \omega \end{bmatrix} + \begin{bmatrix} \partial F_I/\partial \omega \\ \partial F_I/\partial \omega \end{bmatrix} \omega \right), \text{ and} \tag{14}$$

$$B(u_L, u_R) = M_{body}^{-1} \left(\begin{bmatrix} \partial F_T/\partial u_L \\ \partial T_T/\partial u_L \end{bmatrix} u_L + \begin{bmatrix} \partial F_T/\partial u_R \\ \partial T_T/\partial u_R \end{bmatrix} u_R \right). \tag{15}$$

Note that the system matrix is non-linear due to equations 11 and 12.

The state-space system operates in discrete time, with the wingbeat period as the discrete time step. Using the system and control matrices, the body's linear and angular velocity are updated at each time step. The body quaternion and position are updated using the quaternion derivative and body velocity in the inertial reference frame. The values for body mass and velocity have 9 orders of magnitude difference, we therefore needed to rescale these variables to prevent singular matrices. We use three variables for the non-dimensionalization: body mass, $m = 1.16 \cdot 10^{-6}\ kg$, gravitational acceleration, $g = 9800\ mm/s^2$, and wing length, $R = 2.62\ mm$ (Extended Data Table 3).

Model Predictive Control simulations

To simulate free flight maneuvers, we integrated our non-linear discrete-time state-space system of the fly into a Model Predictive Control[62] (MPC) loop using the do-mpc Python package[36] (Extended Data Figure 8). Each MPC simulation involved defining a start state (x_{init}), a goal state (x_{goal}), and a time period (10 wingbeats) for the maneuver execution. The optimization process computed the trajectory that minimizes

the mse between the current state and the goal state, aiming to reach the goal state in the shortest possible time.

The MPC controller utilized dynamic programming to optimize the state-space trajectory over a finite horizon, considering the objective cost function and non-linear constraints. In our simulations, the finite horizon was set to 10 wingbeats, ensuring continuous trajectory computation toward the goal state. The control inputs were the activity patterns of the left and right steering muscles. We restricted the muscle activity patterns based on the correlation analysis shown in Extended Data Figure 5. Specifically, we limited the steering muscle activity to lie within 10% of the normalized 12D muscle activity plane for both wings. The muscle activity of each muscle was also bounded between -0.2 and 1.2. The histograms in Fig. 4. show that the b2 and iii1 muscles are seldom active. We therefore assigned penalization weights to the control parameters: the penalization weight for each muscle was set to 1, with the exception of values of 2 and 10 for muscles b2 and iii1, respectively. In a similar fashion, the importance of the different components of the objective function can be adjusted by setting weights. For instance, for symmetrical maneuvers, we assigned higher weights to state variables that break symmetry, such as v_y and ω_x.

Latent variable analysis

We employed an adapted autoencoder architecture for latent variable analysis[4], where the latent variables predicted both muscle activity and wing motion (Extended Data Figure 9a). The encoder part of the autoencoder split the input data into five streams, each processed by a separate CNN to project onto an individual latent variable. The muscle activity decoder reconstructed the input matrix using a fully-connected dense layer with hyperbolic tangent (tanh) activation and a deconvolutional layer with SELU activation. To focus on the effects of sclerite state on wing kinematics, we introduced a back-propagation stop between the latent space and the muscle activity decoder. Instead of relying on the muscle activity reconstruction error, we used the wing kinematics decoder's reconstruction mse to update the encoder weights.

The wing kinematics decoder utilized a dense layer of 1024 neurons with SELU activation to predict the 80 Legendre coefficients representing wing motion during a wingbeat. After training the latent network for 1000 epochs with mse as the error function, the training error for wing kinematic reconstruction was $\mathrm{mse} = 6.0 \cdot 10^{-4}$, and the validation error was $\mathrm{mse} = 7.9 \cdot 10^{-4}$. The variation of muscle activity per latent parameter, as predicted by the muscle activity decoder, aligned well with the correlation analysis in Extended Data Figure 5. Notably, the i1 and i2 muscles exhibited strong correlation in both the correlation and latent analyses. The anti-correlated activity of b1 and b2 with respect to b3 in the basalare muscles can be explained by the sclerite anatomy. The wing motion derived from virtual experiments in Figure 4 also corresponded to the results of the latent variable analysis (Extended Data Figure 9c). Besides sclerite functionality, the latent variable analysis also predicts the effect of wingbeat frequency on wing motion. Our analysis predicted a decrease in stroke amplitude and downstroke-to-upstroke ratio for increasing frequency, consistent with a study on the power requirements of forward flight[35].

In Extended Data Figure 9d, we present four aerodynamic parameters: absolute angle of attack, wingtip speed, and non-dimensional lift and drag in the SRF, where the quasi-steady model was used to compute lift and drag forces. The computed lift and drag values were lower than the RoboFly measurements in External Data Figures 6 and 7. This discrepancy might be attributed to the omission of wing deformation in the quasi-steady computations.

Wing foot flexion

The latent variable analysis (Fig. 6) predicts a surprising large influence of ax4 on stroke amplitude and deviation, while the anatomical analysis of previous authors suggest only effect on the wing pitch and deformation angles[9]. We hypothesize that the presence of a chord-wise flexure joint at the wing root enables a passive response in stroke and deviation angles to changes in the aerodynamic and inertial forces on the wing. Observations from image sequences during free and tethered flight provided evidence for wingtip extension beyond the morphological limit of the wing root during ventral stroke reversal (Extended Data Figure 10a). Using confocal microscopy, we detected a strong autofluorescence signal with 405 nm excitation (Extended Data Figure 10b), which is consistent with the presence of the elastic protein resilin along a chord-wise line at the base of the wing blade[63]. To assess the extent of bending at the wing root, we use quaternion algebra in combination with the tracked trace of the wing root to compute the deflection angles along the putative chord-wise flexure line. The wing root trace can be expressed by two angles relative to a fixed joint location on the thorax: the wing root stroke angle (ϕ_r) and wing root deviation angle (θ_r). We define a quaternion (q_γ) at the flexure joint that describes the deflection angle along three orthogonal axes (Extended Data Figure 10d). Using the quaternion conjugate, we computed q_γ from ϕ_r, θ_r, η, ϕ and θ. The largest component of q_γ appears to be along the x-axis (Extended Data Figure 10d), which corresponds the proposed flexure line in Extended Data Fig. 10b,c. This chord-wise flexion joint near the wing root can explain the large effect of ax4 on the stroke and deviation angles.

Our latent variable analysis predicts that iv1 and iv2 activity increases the angle of attack during the downstroke, thereby raising the aerodynamic drag on the wing and lowering its velocity (Extended Data Figure 9d). Lower wing velocity and a high angle of attack would result in a smaller lift force on the wing, thereby lowering the deviation angle during the downstroke as the moment around the wing flexure joint is reduced. The ventral extent of stroke amplitude is reduced as well, because the momentum of the wing is lower, which would also reduce the moment about the flexure joint. During stroke reversal, the wing flips over, but the moment about the flexure line remains low during the upstroke due to the reduction in stroke amplitude, which has a profound effect on wing velocity. In summary, the existence of the flexure line at the base of the wing blade could explain why active changes in angle of attack could lead to passive alterations in the trajectory of the wing tip.

Activation of the iv3 and iv4 muscles would have the opposite effect on stroke and deviation angles. At the start of the downstroke, the angle of attack is reduced, thereby lowering the aerodynamic drag on the wing. As a consequence, the wing's velocity and lift increase during the downstroke, elevating the moment about the flexure line and pulling the tip trajectory upward. The ventral extent of stroke amplitude increase, due to the higher wing momentum, increasing wing velocity during the upstroke as well. The higher wing velocity during the upstroke results in higher lift forces and an elevated deviation angle of the wing.

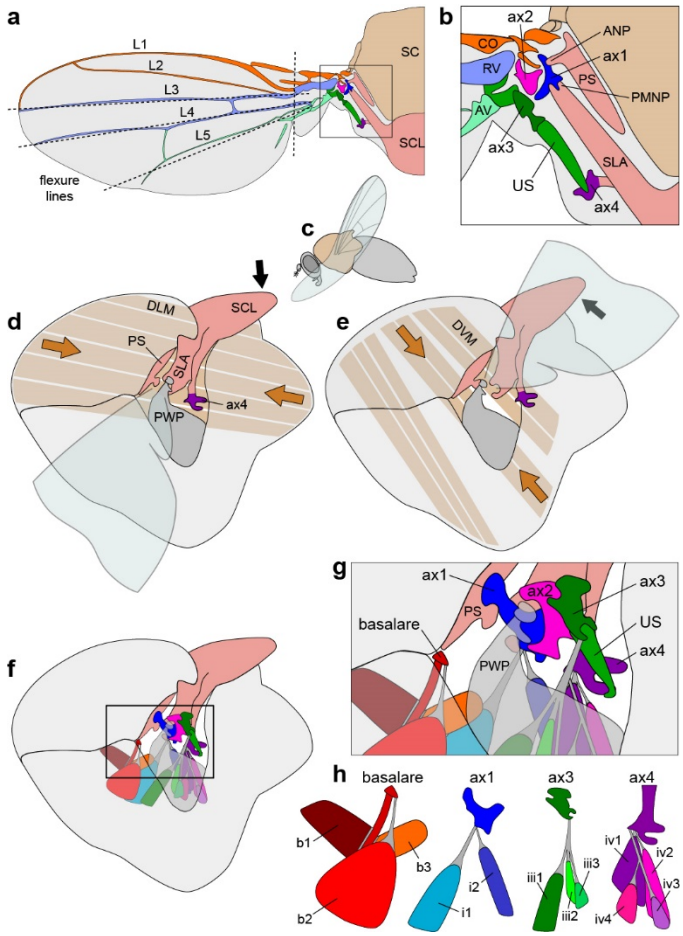

Figure 1 | The wing hinge of a fly is actuated by large power muscles and controlled by small steering muscles. The schematic drawings are based on a synthesis of prior work[2,7-18]. **a,** Schematic top view of the thorax, hinge, and wing, illustrating wing veins (L1-5), scutum (SC), and scutellum (SCL). Dotted lines represent hypothesized flexure lines on the wing. **b,** Close-up of the wing hinge highlighting the parascutal shelf (PS), anterior notal process (ANP), scutellar lever arm (SLA), posterior-medial notal process (PMNP), first, second, third, and fourth axillary sclerites (ax1, ax2, ax3, ax4), costal vein (CO), radial vein (RV), anal vein (AV), and a previously unnamed sclerite (US). **c,** Side view of a flying fly indicating orientation for remaining panels. **d,** Contraction of the dorso-longitudinal muscles (DLMs) causes the scutellum (SCL) to move downward. **e,** Contraction of the dorso-ventral muscles (DVMs) cause the SCL to move upward. These motions are transferred to the wing hinge via the PS and SLA, with the wing's fulcrum located on the pleural wing process (PWP). **f,** Layout of the steering muscles and sclerites in the thorax. **g,** Close-up view of the basalare, axillary sclerites, and steering muscles. Tendons are marked in gray. **h,** Steering muscles grouped according to the sclerite to which they attached: basalare (b1, b2, b3), first axillary (i1, i2), third axillary (iii1, iii2, ii3), and fourth axillary (iv1, iv2, iv3, iv4) muscles.

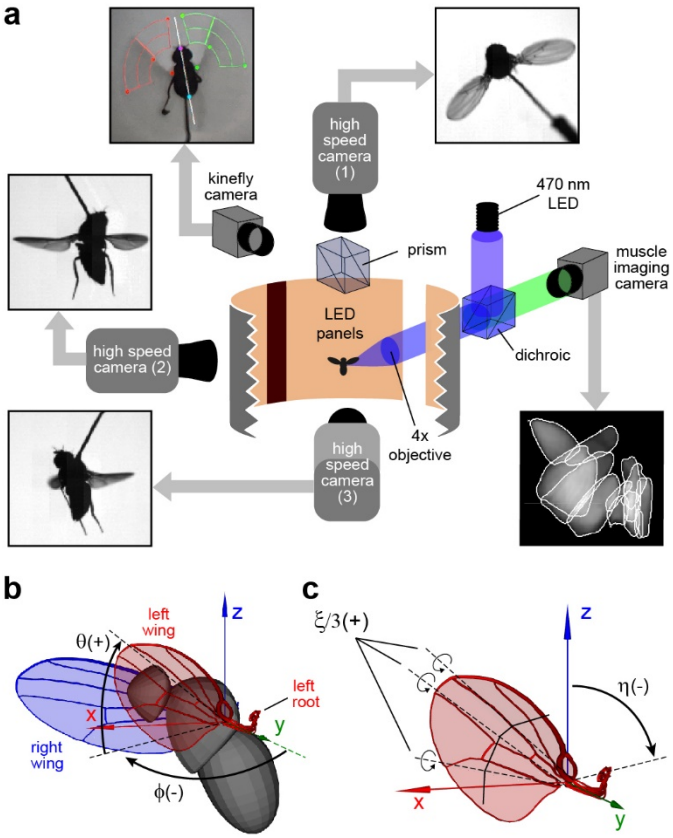

Figure 2 | Simultaneous imaging of muscle activity and wing motion. a, Three high-speed cameras with IR-backlighting capture a tethered fly from three orthogonal angles. An epifluorescence microscope projects blue light onto the left side of the fly's thorax for imaging muscle activity using GCaMP7f. Visual stimuli are provided by an array of orange LED panels surrounding the fly. A prism splits the top view between a high-speed camera and a lower-speed camera that tracks the stroke amplitude of the two wings. **b,** Wing pose is determined from the high-speed camera footage using custom machine vision software. The wing state is subsequently described by four angles relative to the Strokeplane Reference Frame (SRF). The SRF is established by performing principal component analysis (PCA) on the motion of the left and right wing roots, with the x-y plane representing the mean strokeplane. Two angles, φ (stroke angle) and θ (deviation angle), describe the wing's orientation in the SRF (the +/- sign indicates the direction of rotation). **c,** The wing pitch angle, η, indicates the orientation of the leading edge relative to the z-axis of the SRF. The deformation angle, ξ, represents the uniform rotation along three hinge lines that roughly align with the L3, L4, and L5 veins.

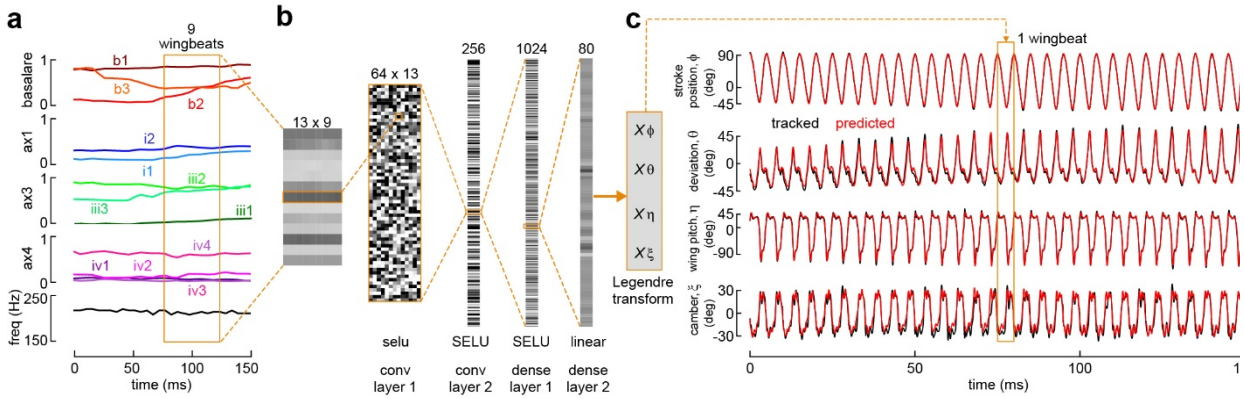

Figure 3 | A trained CNN predicts wing motion from steering muscle activity and wingbeat frequency. a, Muscle activity recording displaying normalized muscle fluorescence (grouped according to sclerite) and wingbeat frequency. **b,** The trained CNN takes a 13x9 matrix as input, consisting of normalized muscle fluorescence and wingbeat frequency data over a temporal window of 9 wingbeats. Two convolutional (conv) layers with SELU activations extract features from the input matrix. A fully connected (dense) layer with 1024 neurons learns the relationships between the extracted features and an output layer of 80 neurons with linear activations. These 80 neurons correspond to 80 Legendre coefficients, encoding the four wing kinematic angles during the first wingbeat in the 9-wingbeat window. The wing kinematic can be reconstructed by multiplying the Legendre coefficients with the corresponding Legendre basis functions (Xφ, Xθ, Xη, Xξ). **c,** Comparison between predicted (red) and tracked (black) traces of the four wing kinematic angles throughout the example recording.

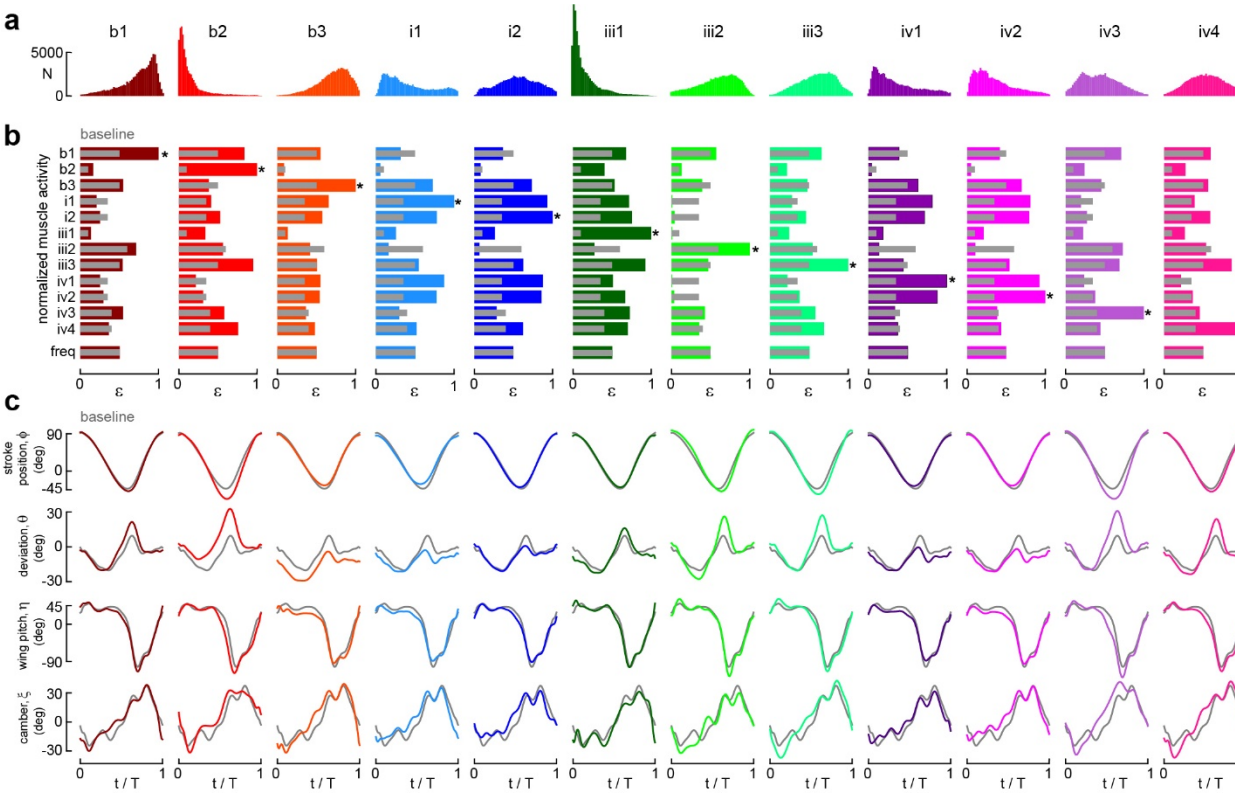

Figure 4 | Modulation of wing motion by steering muscle activity revealed through virtual experiments. a, Distribution of normalized muscle activity (ϵ) for all 12 steering muscles. **b,** Maximum muscle activity patterns (colored bars) for each steering muscle. These patterns were obtained by transitioning from the baseline activity pattern (gray) to the maximum activity (ϵ=1) of a specific muscle on the 12-dimensional muscle activity plane (see Extended Data Figure 5). Wingbeat frequency is maintained at a constant level for all patterns. **c,** CNN-predicted wing kinematics for the baseline and maximum activity patterns shown in (b) over a single wingbeat period (T). The kinematics from the baseline muscles activity patterns are shown in gray; the colored lines represent the kinematics resulting from the maximum activity patterns of the corresponding muscles.

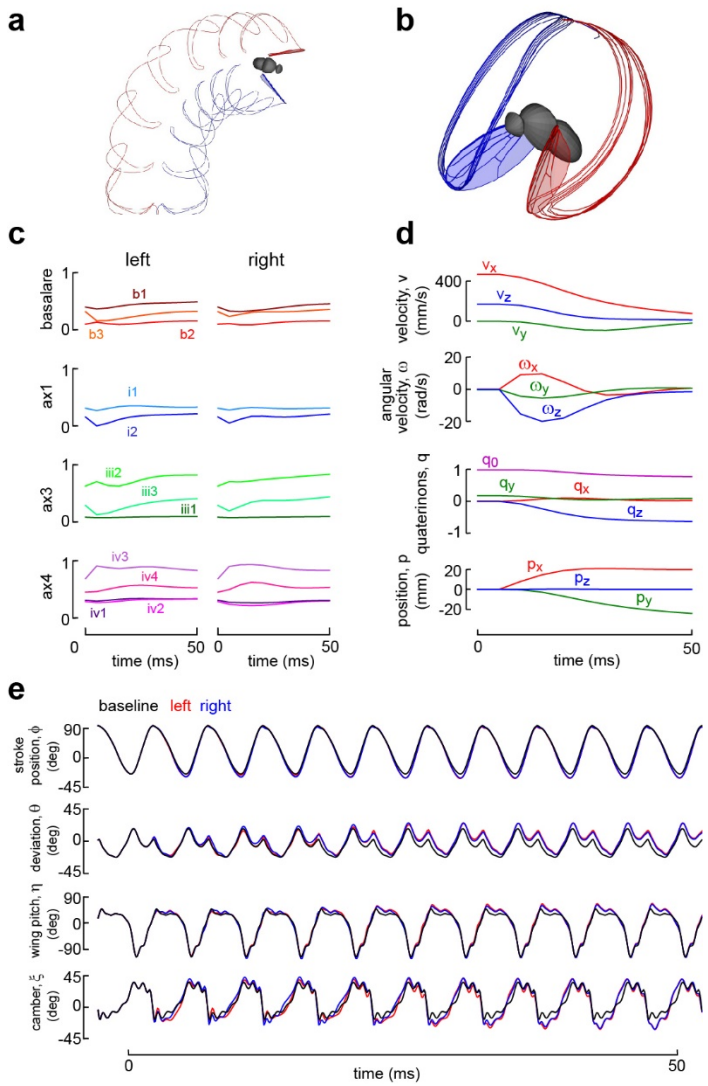

Figure 5 | Model Predictive Control (MPC) simulation of a rightward saccade. a, Top view of a 30 ms simulation, showing red and blue traces for the left and right wingtips, respectively. **b,** Orthographic view of wingtip traces of the simulation in a stationary body frame. **c,** Control inputs during the saccade, representing the activity of left and right steering muscles, grouped according to sclerite. **d,** Body state during the saccade, including linear (v) and angular (ω) velocities in the SRF, as well as body quaternion (q) and position (p) relative to an inertial reference frame. **e,** CNN-predicted wing kinematic angles derived from the steering muscle activity in (c). Left wing motion is indicated in red, right wing motion in blue. The baseline wingbeat (black) is repeated throughout the maneuver for comparison. Additional MPC simulation results can be found in Extended Data Figure 8.

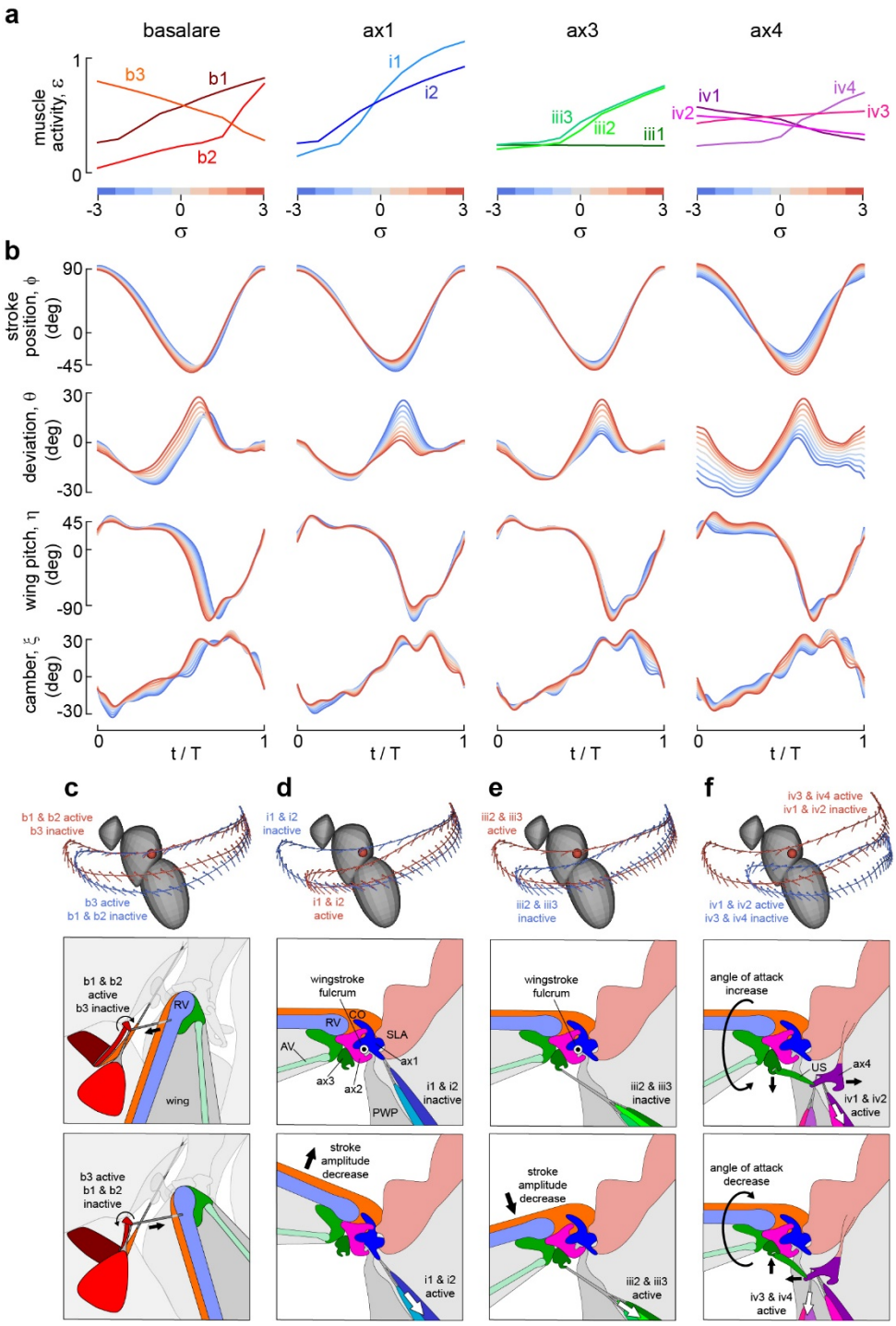

Figure 6 | Latent variable analysis reveals the role of sclerite function in the control of wing motion. a, Steering muscle activity predicted by the muscle activity decoder as a function of the sclerite latent parameters (see extended Data Figure. 9). The z-scored latent variables representing each sclerite state were sampled in 9 steps, ranging from -3σ to +3σ (σ = standard deviation) and indicated by color bars. **b,** Wing kinematic angles predicted by the wing kinematics decoder, showing their dependence on sclerite state. The colors of the 9 traces correspond to the color bars in (a). **c,** Patterns of wing motion corresponding to extreme sclerite states (-3σ, blue; +3σ, red). Each figure plots the instantaneous wing pitch angle and wing deformation angle at regular intervals superimposed over the wingtip traces. The leading edge of the wing is indicated by a circle, and the wing's cross-section is represented by a curved line that shows camber. **c,** Cartoon illustrating proposed mechanism of action for the basalare, drawn for a left wing from an external view. The b1 and b2 rotate the basalare clockwise, exerting tension on a ligament attached to the base of the radial vein (RV), extending the wingstroke forward and advancing wing supination during the downstroke and ventral stroke reversal. The b3 rotates the basalare counter-clockwise and has the opposite effects. **d,** Cartoon illustrating proposed action of ax1 drawn for a left wing in cross section through the winge hinge. Contraction of the i1 and i2 muscles pull ax1 ventrally, resulting in a decrease in the extent of the ventral stroke due to the inboard position of ax1 relative to ax2. **e,** Same view as in (d). illustrating action of ax3. The iii2 and iii3 muscles pull ax3 ventrally, causing an increase in the ventral stroke extent due to its outboard position relative to ax2. **f,** Same view as in (e), illustrating action of ax4. Ax4 is connected to ax3 and the Anal Vein (AV) via a long unnamed sclerite (US). The iv1 and iv2 muscles pull ax4 inward, leading to an increased angle of attack during the downstroke via the ax4-US-ax3-AV linkage. The iv3 and iv4 muscles pulls ax4 outward, reducing the angle of attack during the downstroke.

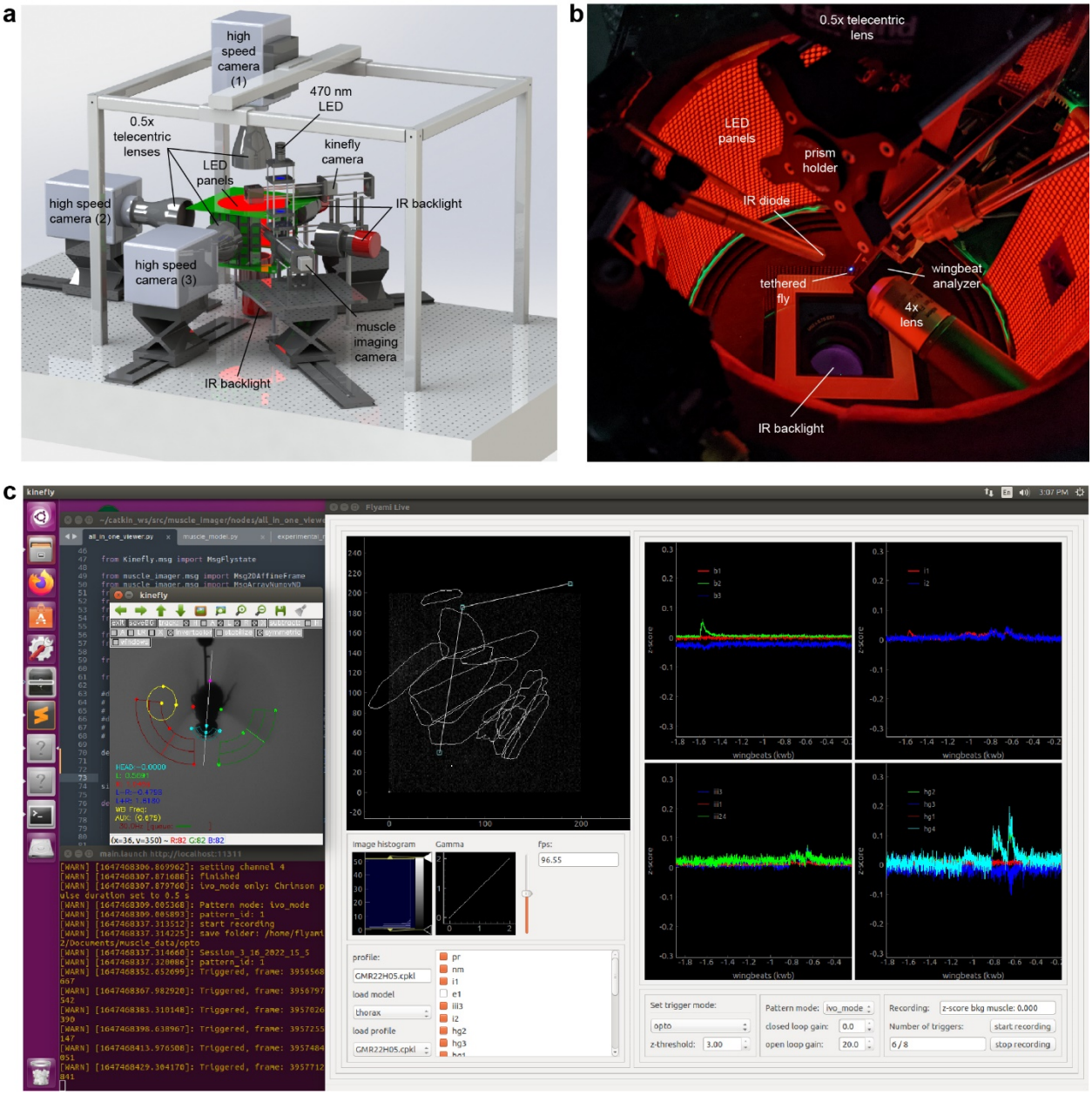

Extended Data Figure 1 | Automated setup for simultaneous recording of muscle fluorescence and wing motion. **a,** High-speed cameras, equipped with 0.5X telecentric lenses and collimated IR back-lighting, capture synchronized frames of the fly from three orthogonal angles at a rate of 15,000 fps. An epi-fluorescence microscope with a muscle imaging camera records GCaMP7f fluorescence in the left steering muscles at approximately 100 fps, utilizing a strobing mechanism at half the wingbeat frequency. A blue LED provides a brief, 1 ms illumination of the fly's thorax during dorsal stroke reversal. A camera operating at 30 fps captures a top view of the fly for the kinefly wing tracker. **b,** Image of the flight arena featuring the components of the setup: LED panorama, IR diode and wingbeat analyzer for triggering the muscle camera and blue LED, prism for splitting the top view between HS camera 3 and the kinefly camera, IR backlight, 4X lens of the epi-fluorescence microscope, and a tethered fly illuminated by the blue LED. **c,** Screenshot of the ROS-system (Robot Operating System) and graphical user interface used for automated muscle activity extraction and triggering the recording of a 1.1-second high-speed video centered around each muscle trigger event. The kinefly system automatically extracts left and right stroke amplitudes to provide feedback for closed-loop visual stimuli displayed on the LED wall.

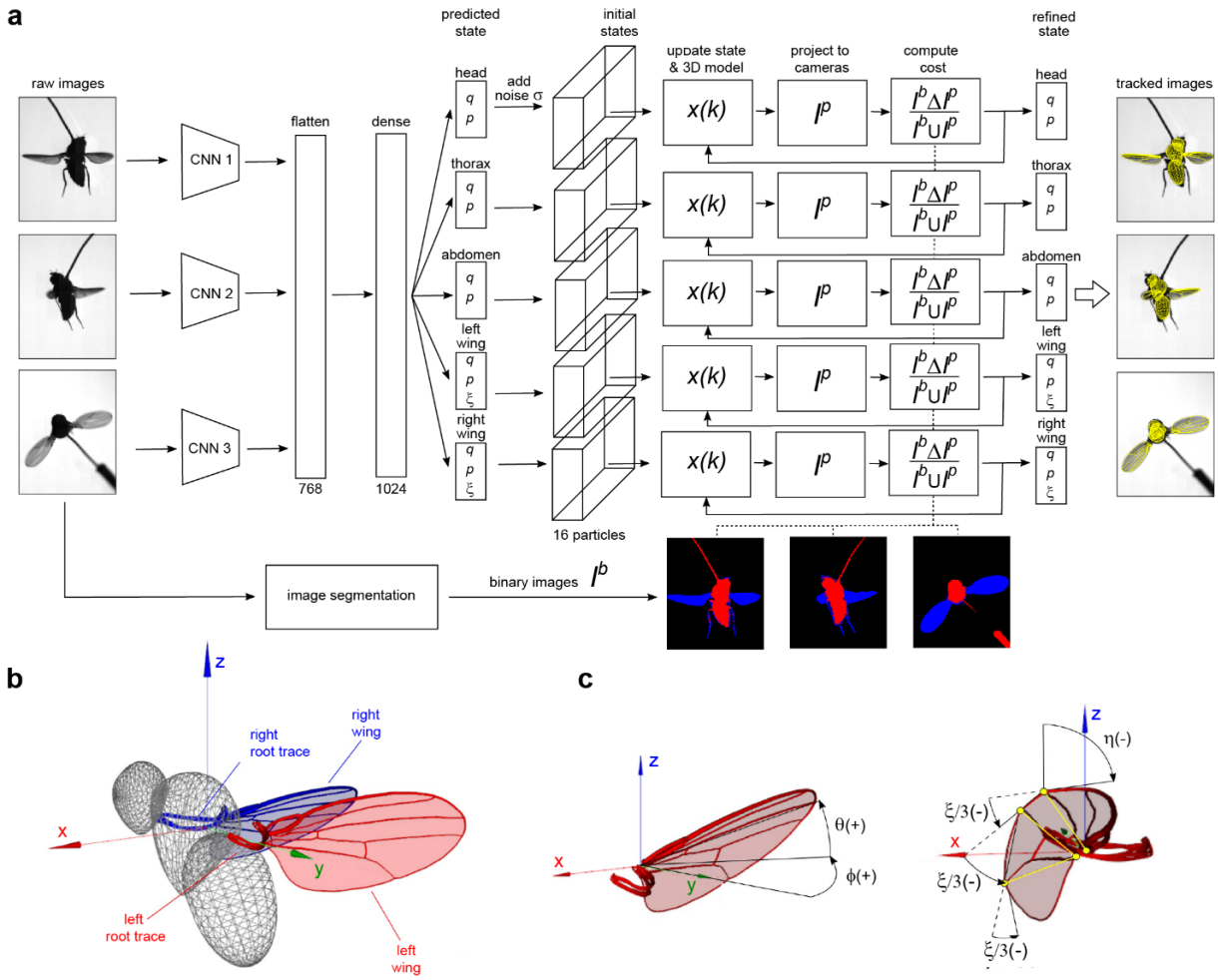

Extended Data Figure 2 | FlyNet workflow and definitions of wing kinematic angles. a, The FlyNet algorithm takes three synchronized frames as input. Each frame undergoes CNN processing, resulting in a 256-element feature vector extracted from the image. These three feature vectors are concatenated and analyzed by a fully connected (dense) layer with Scaled Exponential Linear Unit (SELU) activation, consisting of 1024 neurons. The output of the neural network is the predicted state (37 elements) of the five model components represented by a quaternion (q), translation vector (p), and wing deformation angle (ξ). Subsequently, the state vector is refined using 3D model fitting and particle swarm optimization (PSO). Normal distributed noise is added to the predicted state, forming the initial state for 16 particles. During the 3D model fitting, the particles traverse the state-space, maximizing the overlap between binary body and wing masks of the segmented frames (I^b) and the binary masks of the 3D model projected onto the camera views (I^p). The cost function $(I^b \Delta I^p)/(I^b \cup I^p)$ is evaluated iteratively for a randomly selected 3D model component. The PSO algorithm tracks the personal best cost encountered by each particle and the overall lowest cost (global best). After 300 iterations, the refined state is determined by selecting the global best for each 3D model component. **b,** The Strokeplane Reference Frame (SRF) is established through a principal component analysis of the left and right wing root traces, where the first, second, and third principal components correspond to the y, x, and z-axes, respectively. The wing pose is described by four angles: stroke angle (φ), deviation angle (θ), wing pitch angle (η), and wing deformation angle (ξ).

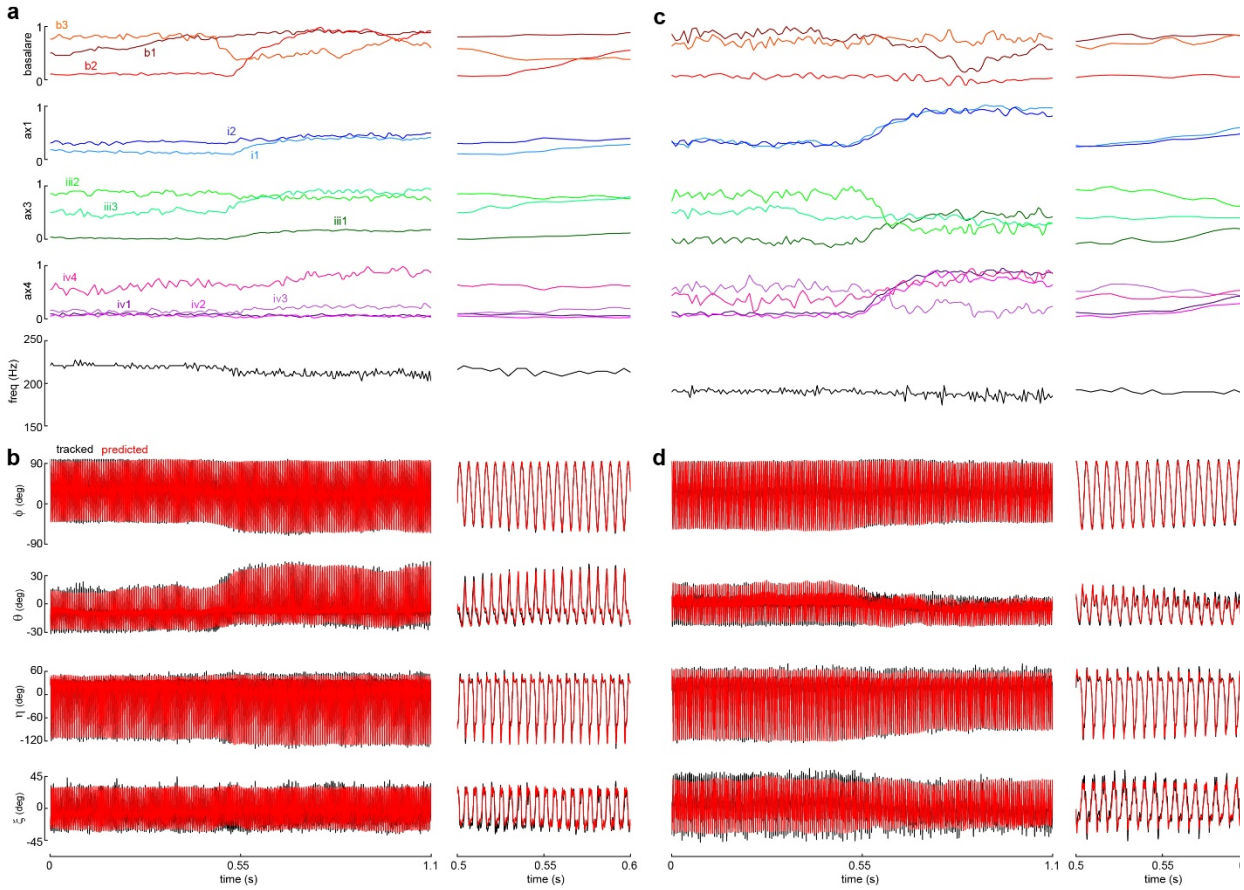

Extended Data Figure 3 | CNN-predicted wing motion for two example flight sequences. a, Steering muscle activity and wingbeat frequency during a full recording and a close-up section (0.5-0.6 seconds) of the high-speed sequence. **b,** Comparison between the tracked (black) and CNN-predicted (red) wing kinematic angles throughout the high-speed video. **c, d,** Same as (a) and (b) but for a different flight sequence. See also Fig. 3.

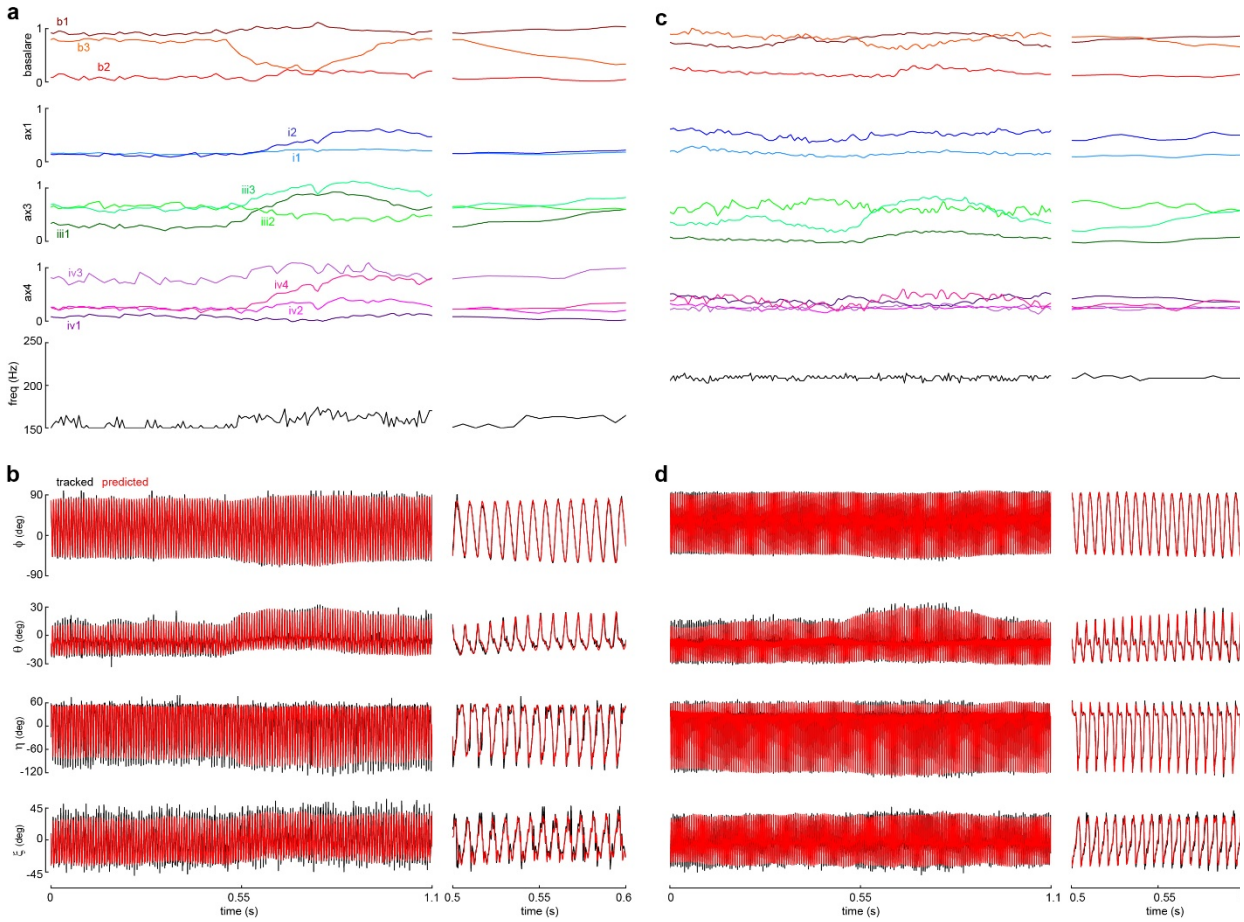

Extended Data Figure 4 | CNN-predicted wing motion for two example flight sequences. a, Steering muscle activity and wingbeat frequency during a full recording and a close-up section (0.5-0.6 seconds) of the high-speed sequence. **b,** Comparison between the tracked (black) and CNN-predicted (red) wing kinematic angles throughout the high-speed video. **c, d,** Same as (a) and (b) but for a different flight sequence. See also Fig. 3. and Extended Data Figure 4.

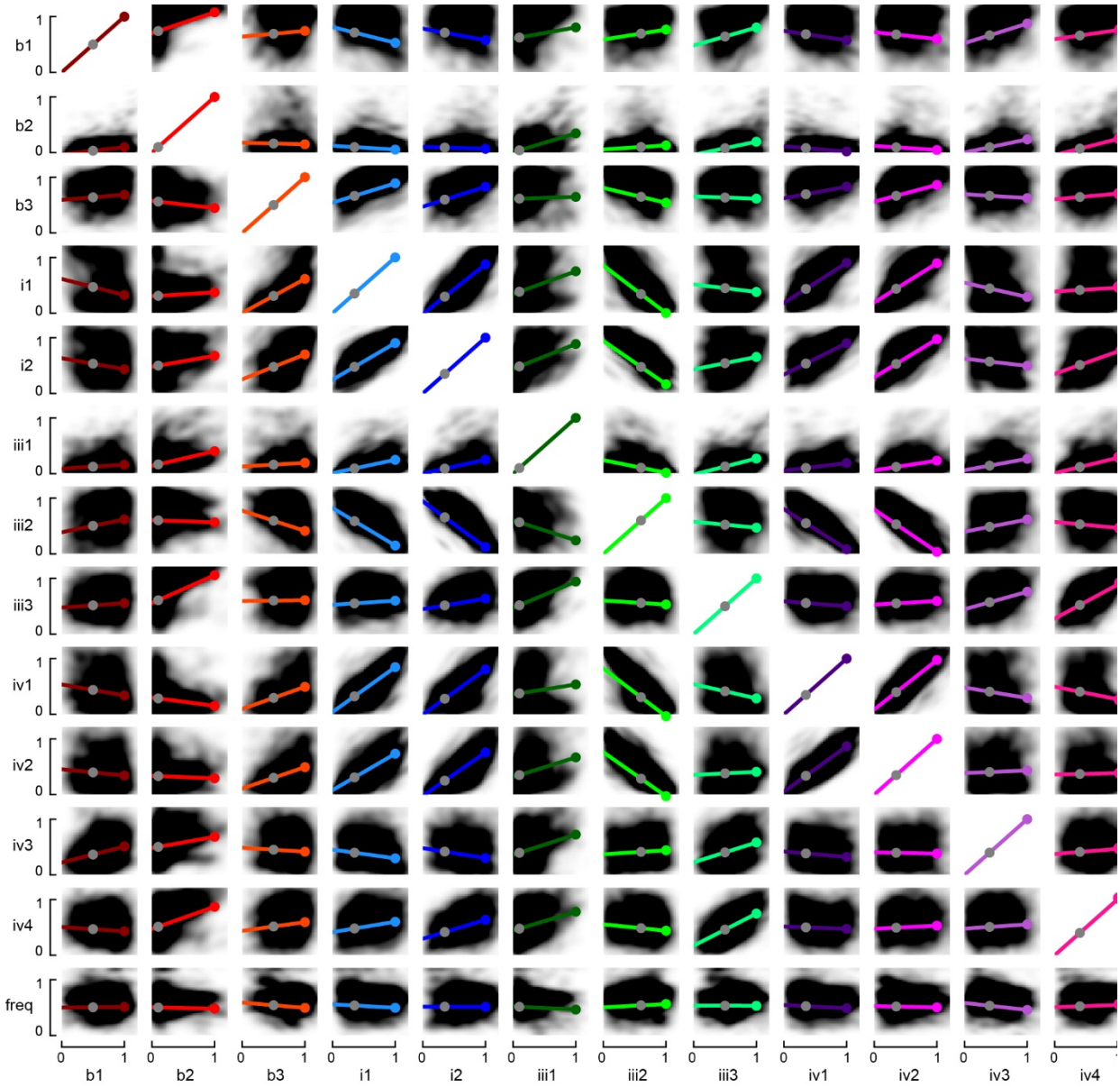

Extended Data Figure 5 | Correlation analysis of steering muscle fluorescence and wingbeat frequency. Linear models (colored lines) fitted to wingbeats in the entire dataset of 76,270 wingbeats from 82 flies, for which the fluorescence of a specific muscle (column) had a fluorescence gradient larger than 0.005. Gray dots represent the baseline muscle activity pattern, while colored dots represent the maximum muscle activity patterns. The bias of the linear models has been adjusted to include the baseline muscle activity pattern.

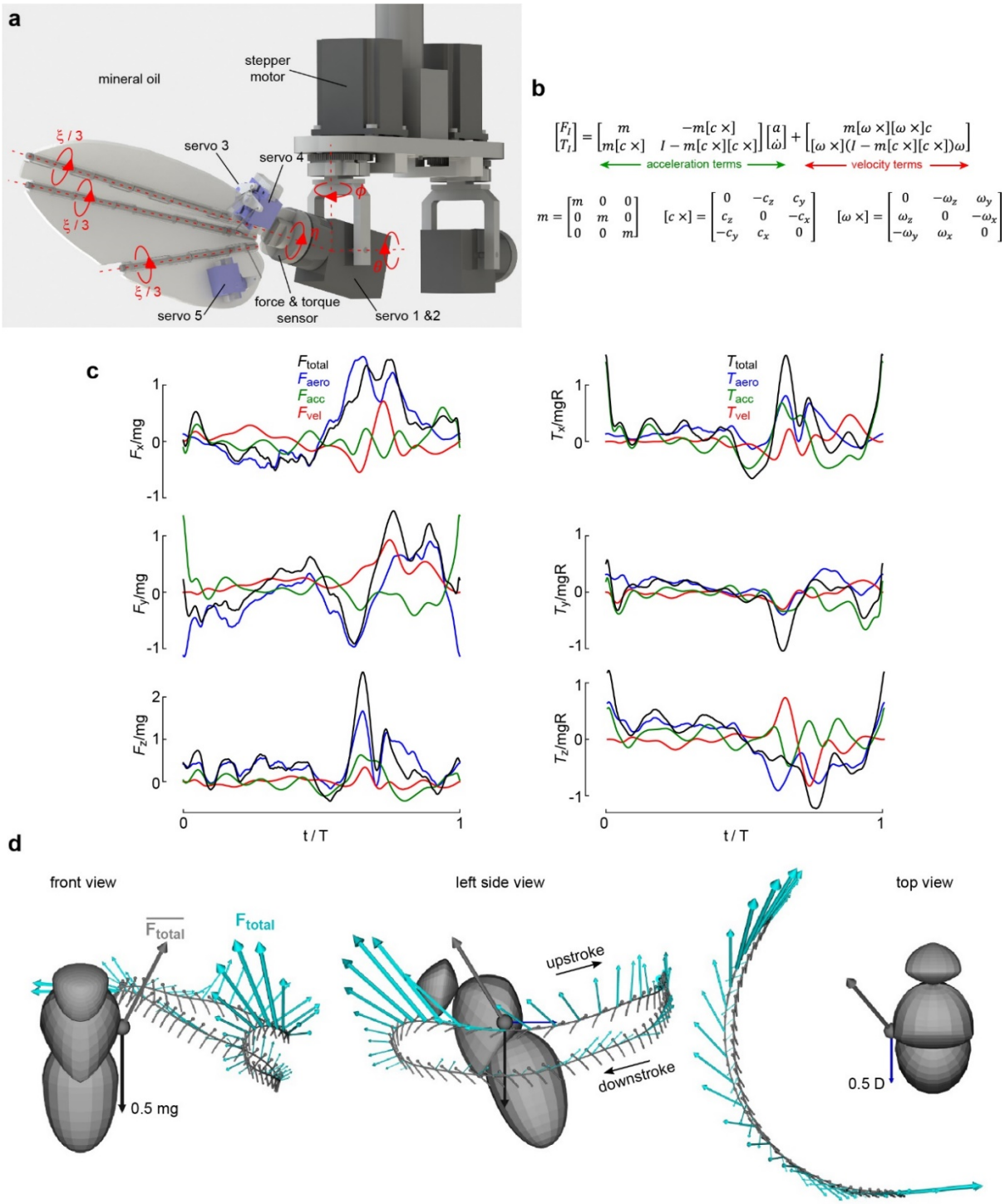

$$\begin{bmatrix} F_l \\ T_l \end{bmatrix} = \begin{bmatrix} m & -m[c\times] \\ m[c\times] & I - m[c\times][c\times] \end{bmatrix} \begin{bmatrix} a \\ \dot{\omega} \end{bmatrix} + \begin{bmatrix} m[\omega\times][\omega\times]c \\ [\omega\times](I - m[c\times][c\times])\omega \end{bmatrix}$$

$$m = \begin{bmatrix} m & 0 & 0 \\ 0 & m & 0 \\ 0 & 0 & m \end{bmatrix} \quad [c\times] = \begin{bmatrix} 0 & -c_z & c_y \\ c_z & 0 & -c_x \\ -c_y & c_x & 0 \end{bmatrix} \quad [\omega\times] = \begin{bmatrix} 0 & -\omega_z & \omega_y \\ \omega_z & 0 & -\omega_x \\ -\omega_y & \omega_x & 0 \end{bmatrix}$$

Extended Data Figure 6 | Aerodynamic force measurements and inertial force calculations. a, RoboFly setup immersed in mineral oil. **b,** The Newton-Euler equations consist of two components: forces and torques due to acceleration and rotational velocity. A 3x3 mass tensor (m) and the cross-products of the center of mass ($[c\times]$) and angular velocity ($[\omega\times]$) are also depicted. **c,** Non-dimensional forces and torques in the SRF for the baseline wingbeat. **d,** Representation of total forces during the baseline wingbeat, viewed from the front, left, and top. Gray trace represents the wing trajectory; cyan arrows represent instantaneous total force on the wing. At the wing joint, three arrows depict the total mean force, half the body weight, and half the estimated body drag.

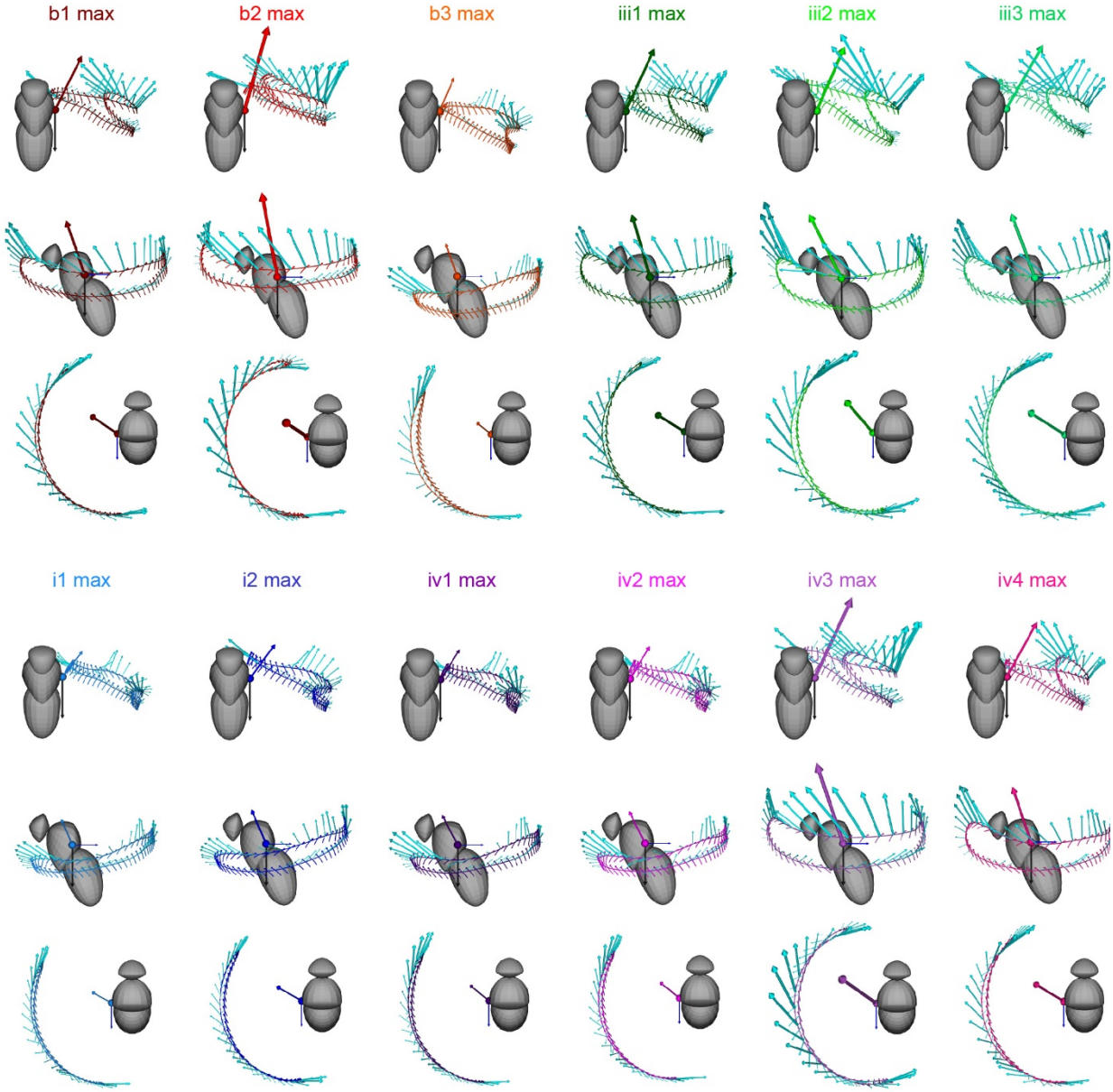

Extended Data Figure 7 | Aerodynamic and inertial forces for maximum muscle activity wingbeats. Figures depict the CNN-predicted wing motion for maximum muscle activity patterns, viewed from the front, left side, and top. Instantaneous vectors depicting the sum of aerodynamic and inertial forces are shown in cyan. The wingbeat-averaged force vector is indicated by the color corresponding to the specific steering muscle with maximum activity. It should be noted that the scaling for the wingbeat-averaged forces differs from that for the instantaneous forces. The black gravitational force and blue body drag force are consistent with Extended Data Fig. 6.

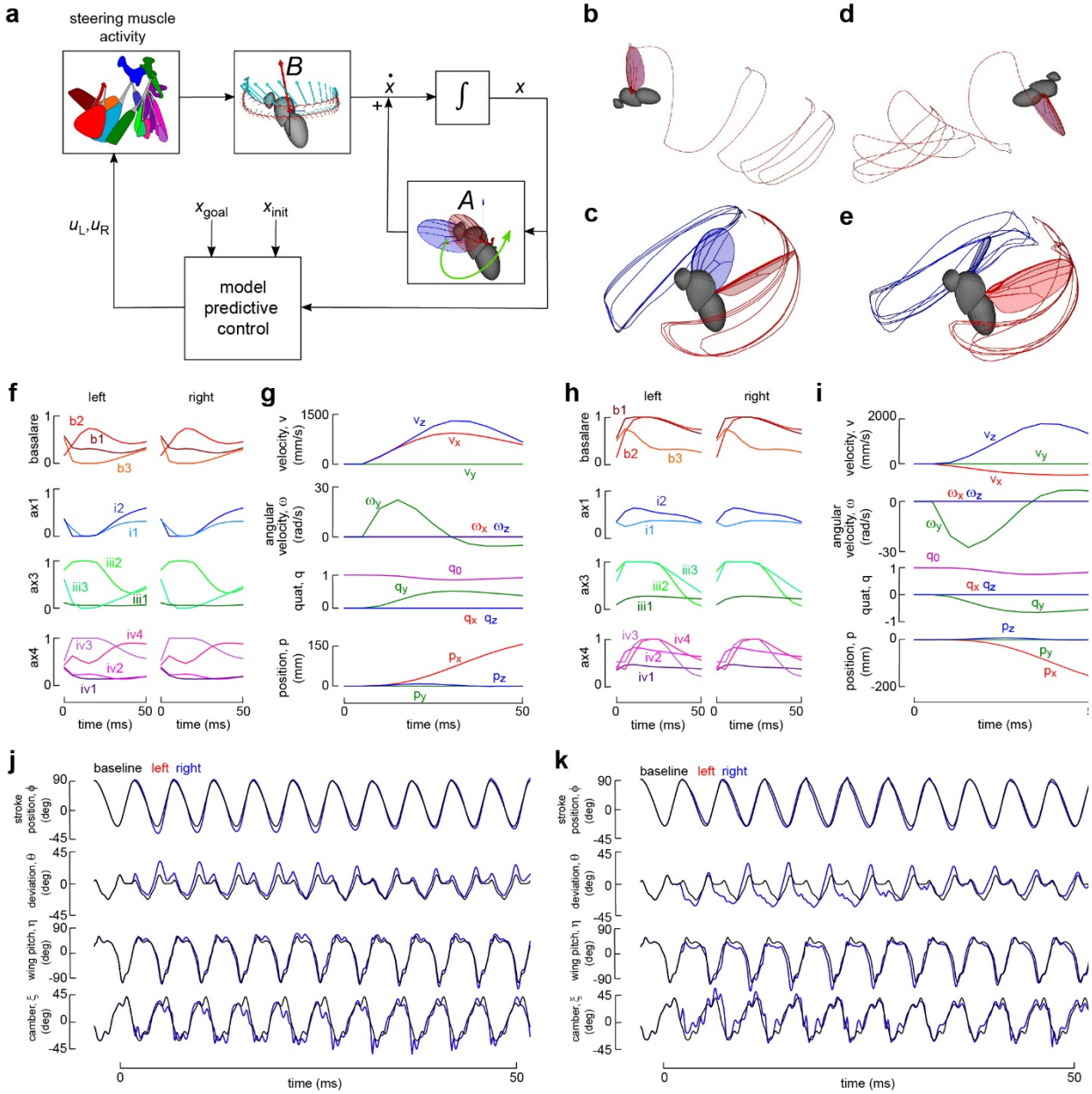

Extended Data Figure 8 | Simulation of free flight maneuvers using the state-space system in a Model Predictive Control. a, Schematic of the state-space system and MPC loop, including system matrix (A), control matrix (B), state vector (x), temporal derivative ($\dot{x}$), left and right steering muscle activity (u_L, u_R), initial state (x_{init}), and goal state (x_{goal}). **b,** Forward flight simulation with wingtip traces in red and blue. **c,** Wing motion during forward flight simulation plotted in stationary body frame. **d,** Backward flight simulation. **e,** Wing motion during backward flight simulation plotted in stationary body frame. **f,** Left and right steering muscle activity during the forward flight maneuver. **g,** State vector during forward flight maneuver. **h,** Steering muscle activity for the backward flight maneuver. **i,** State vector for the backward flight maneuver. **j,** CNN-predicted left (red) and right (blue) wing kinematics for the muscle activity in (f). Note that the left wing kinematics are displayed underneath the right kinematics, and a baseline wingbeat is shown to emphasize the relative changes in wing motion. **k,** CNN-predicted wing motion for the backward flight maneuver.

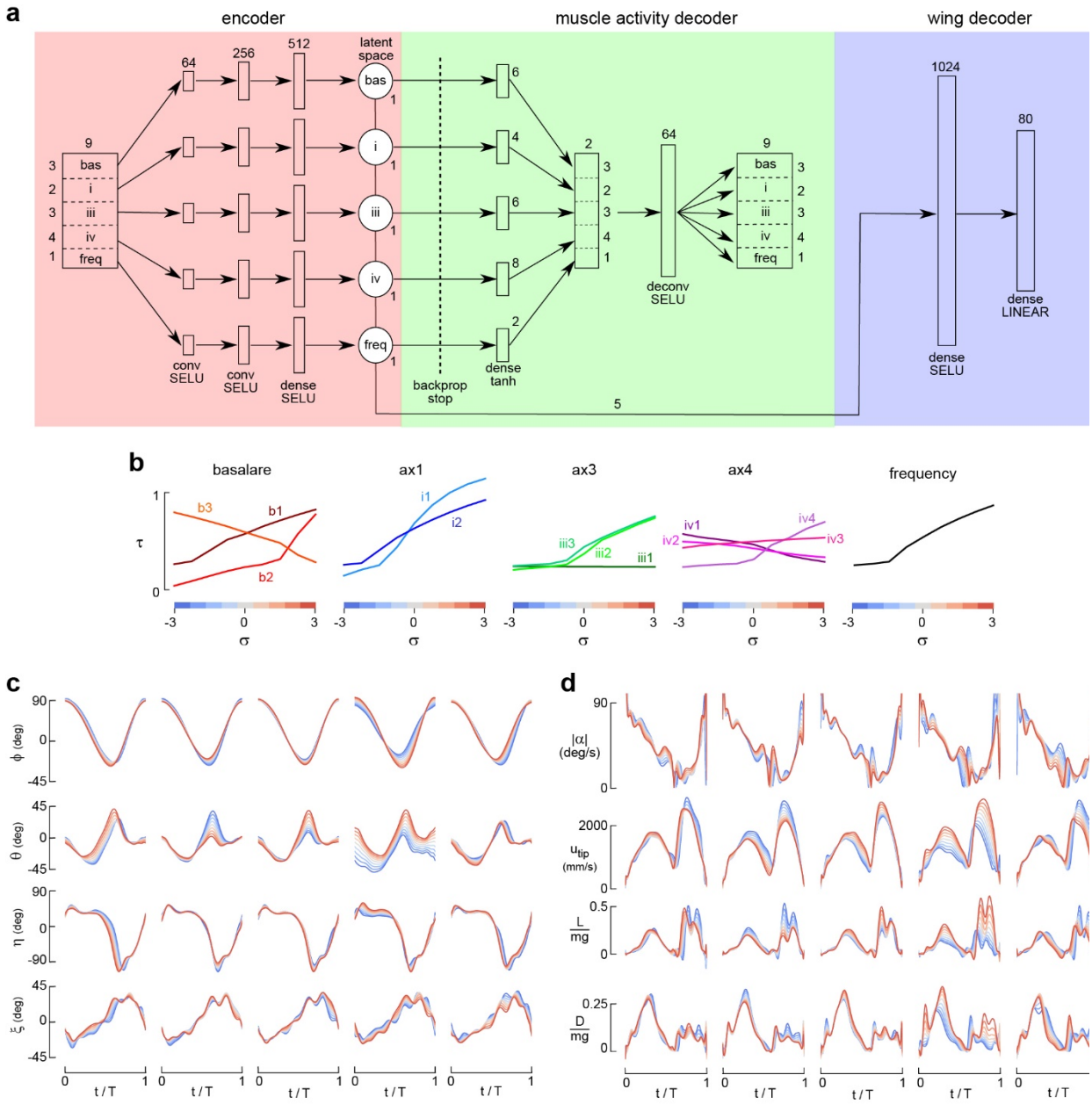

Extended Data Figure 9 | Latent variable analysis reveals sclerite function using an autoencoder CNN. a, The autoencoder architecture consists of an encoder (red), muscle activity decoder (green), and wing kinematics decoder (blue). The encoder splits the input data into five streams corresponding to different muscle groups and frequency. Feature extraction is performed using convolutional and fully connected layers with SELU activation. Each stream is projected onto a single latent variable. In the muscle activity decoder, the latent variables are transformed back into the input data. A backpropagation stop prevents weight adjustments in the encoder based on the muscle activity reconstruction. The wing kinematics decoder predicts the Legendre coefficients of wing motion using the latent variables. **b,** Predicted muscle activity and wingbeat frequency as a function of each latent parameter varied within the range of -3σ to +3σ. Color bar indicates the latent variable value in panels (c) and (e). **c,** Predicted wing motion by the wing kinematics decoder for the five latent parameters. **d,** Absolute angle of attack (|α|), wingtip velocity (u_{tip}) in mm/s, non-dimensional lift (L/mg), and non-dimensional drag (D/mg). The non-dimensional lift and drag were computed using a quasi-steady model.

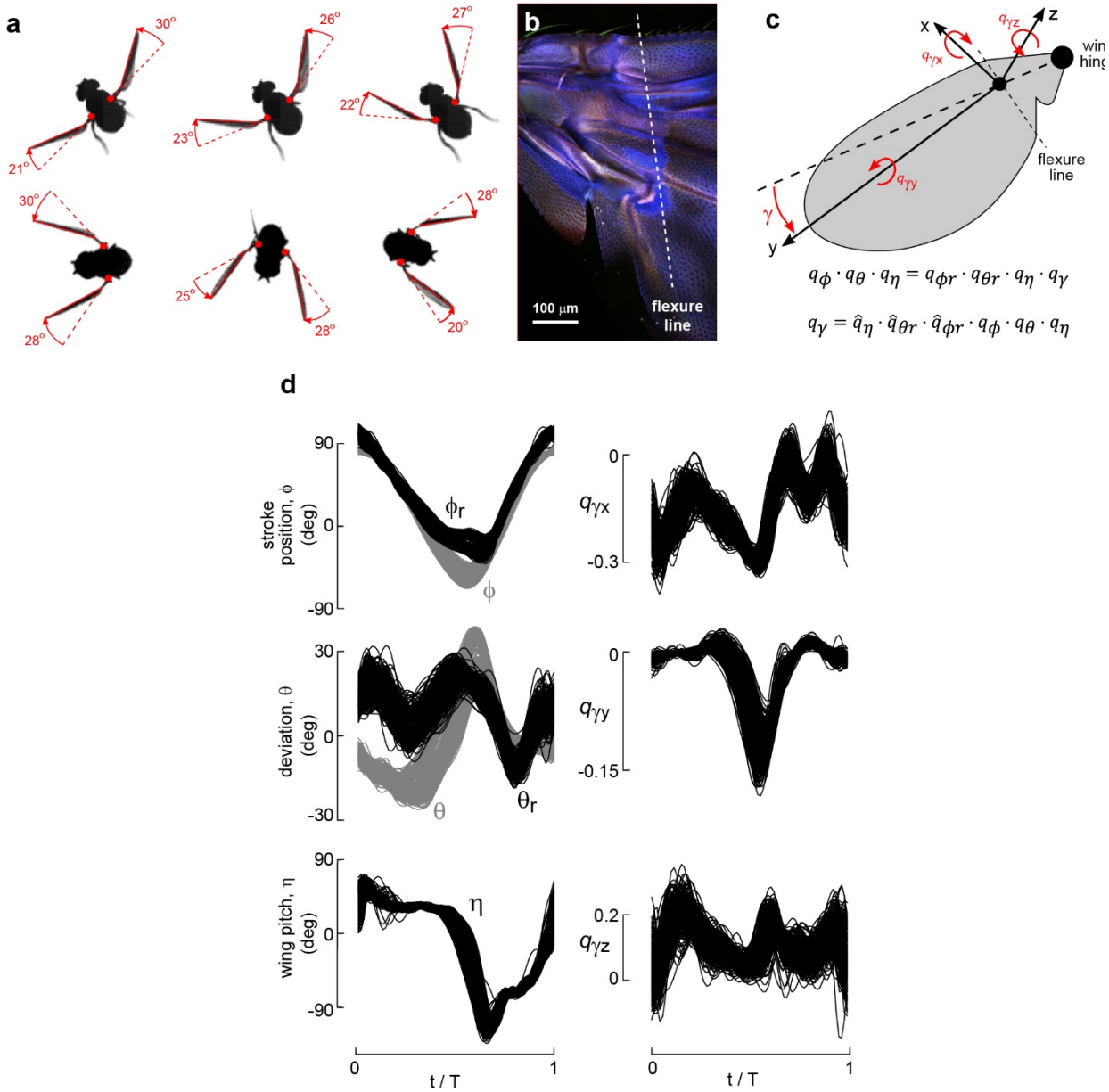

Extended Data Figure 10 | Flexible wing root facilitates elastic storage during wingbeat and allows wing to passively respond to changes in lift and drag throughout stroke. a, Top view of ventral stroke reversal in tethered and free flight. Red circles mark the estimated position of the wing hinge, dotted lines indicate the expected position of the wing if a chord-wise flexure line was not present. Composite confocal image of the wing base, indicating a bright blue band of auto-fluorescence consistent with the presence of resilin and existence of a chord-wise flexure line. **c,** Quaternion algebra enables determination of the quaternion, q_γ, at the wing root, achieving the same wing orientation as the standard φ, θ, η Tait-Bryan sequence. Stroke (φ_r) and deviation (θ_r) angles of the wing root are computed using the wing hinge location and root trajectory, resulting in a φ_r, θ_r, η, γ rotation sequence; q_γ was determined from the quaternion conjugate ($\hat{q}$). **d,** Plots of φ, φ_r, θ, θ_r, η, and the vector components of q_γ ($q_{\gamma x}$, $q_{\gamma y}$, $q_{\gamma z}$) for a video sequence with 230 wingbeats.

Extended Data Tables

Trigger muscle	Number of high-speed movies									
b1	5	2	8	6	8	8	-	-	-	-
b2	4	8	4	7	7	6	1	1	-	-
b3	8	2	8	7	3	7	8	-	-	-
i1	8	3	1	2	8	8	5	8	5	-
i2	6	8	5	6	3	4	8	2	2	-
iii1	4	-	-	-	-	-	-	-	-	-
iii2	8	3	8	6	-	-	-	-	-	-
iii3	8	8	8	8	7	2	8	8	3	8
iv1	6	8	8	4	5	1	3	-	-	-
iv2	8	8	8	8	5	2	5	6	-	-
iv3	8	8	8	1	5	8	8	7	-	-
iv4	8	5	8	8	7	4	-	-	-	-

Extended Data Table 1 | Number of high-speed videos recorded per trigger muscle. Note that each cell states the number of videos per individual fly. In total: 479 movies were collected from 82 flies.

	b1	**b2**	**b3**	**i1**	**i2**	**iii1**	**iii2**	**iii3**	**iv1**	**iv2**	**iv3**	**iv4**	**Base**
b1	1.00	0.38	0.09	-0.27	-0.15	0.21	0.18	0.32	-0.16	-0.09	0.38	0.16	0.50
b2	0.12	1.00	-0.05	-0.07	-0.01	0.34	0.08	0.20	-0.09	-0.07	0.24	0.25	0.10
b3	0.09	-0.14	1.00	0.36	0.36	0.04	-0.27	-0.03	0.22	0.33	-0.07	0.10	0.50
i1	-0.30	0.06	0.60	1.00	0.86	0.41	-0.86	-0.17	0.73	0.73	-0.29	0.05	0.35
i2	-0.20	0.19	0.43	0.65	1.00	0.45	-0.78	0.21	0.56	0.72	-0.16	0.40	0.35
iii1	0.06	0.26	0.04	0.23	0.23	1.00	-0.23	0.23	0.12	0.17	0.18	0.25	0.10
iii2	0.24	-0.03	-0.34	-0.65	-0.79	-0.35	1.00	-0.08	-0.71	-0.78	0.26	-0.09	0.60
iii3	0.08	0.50	-0.01	0.07	0.23	0.46	-0.07	1.00	-0.09	0.09	0.29	0.60	0.50
iv1	-0.20	-0.16	0.39	0.77	0.73	0.16	-0.86	-0.29	1.00	0.90	-0.24	-0.25	0.35
iv2	-0.11	-0.05	0.37	0.62	0.71	0.34	-0.80	0.02	0.79	1.00	0.01	0.01	0.35
iv3	0.30	0.20	-0.08	-0.15	-0.14	0.35	0.07	0.32	-0.09	-0.02	1.00	0.06	0.40
iv4	-0.08	0.40	0.14	0.17	0.36	0.33	-0.11	0.58	-0.06	0.08	0.07	1.00	0.40
f	0.02	0.00	-0.09	-0.06	0.00	-0.02	0.04	-0.01	-0.04	-0.02	-0.08	0.04	0.50
N	7606	4325	8884	7252	6949	599	10772	8727	7457	7347	9154	13699	-

Extended Data Table 2 | Correlation slopes and baseline muscle activity pattern. Each column contains the slopes of the linear model fitted to a subset of wingbeats (N) for which the fluorescence gradient exceeds a threshold (> 0.005). The baseline muscle activity pattern is given on the right.

State vector:

$$x = [v_x \quad v_y \quad v_z \quad \omega_x \quad \omega_y \quad \omega_z \quad q_0 \quad q_x \quad q_y \quad q_z \quad p_x \quad p_y \quad p_z]$$

State derivative:

$$\dot{x} = [a_x \quad a_y \quad a_z \quad \dot{\omega}_x \quad \dot{\omega}_y \quad \dot{\omega}_z \quad \omega_x \quad \omega_y \quad \omega_z \quad v_x \quad v_y \quad v_z]$$

Control vector left:

$$u_L = [b1 \quad b2 \quad b3 \quad i1 \quad i2 \quad iii1 \quad iii2 \quad iii3 \quad iv1 \quad iv2 \quad iv3 \quad iv4]_L$$

Control vector right:

$$u_R = [b1 \quad b2 \quad b3 \quad i1 \quad i2 \quad iii1 \quad iii2 \quad iii3 \quad iv1 \quad iv2 \quad iv3 \quad iv4]_R$$

Scaling parameters:

$$m = 1.16 \cdot 10^{-6}\ kg \qquad R = 2.62\ mm \qquad g = 9800\ mm/s^2$$

Scaling factors:

$$F = 1/mg \qquad T = 1/mgR \qquad a = 1/g \qquad \dot{\omega} = R/g$$
$$v = 1/\sqrt{gR} \qquad \omega = \sqrt{R}/\sqrt{g} \qquad q = 1 \qquad p = 1/R$$

Body inertia tensor:

$$M_{body} = \begin{bmatrix} 1 & 0 & 0 & 0 & 0 & 0 \\ 0 & 1 & 0 & 0 & 0 & 0 \\ 0 & 0 & 1 & 0 & 0 & 0 \\ 0 & 0 & 0 & 0.59 & 0 & 0.16 \\ 0 & 0 & 0 & 0 & 0.67 & 0 \\ 0 & 0 & 0 & 0.16 & 0 & 0.20 \end{bmatrix}$$

Aerodynamic damping:

$$\begin{bmatrix} \frac{\partial F_{aero}}{\partial v} \\ \frac{\partial T_{aero}}{\partial v} \end{bmatrix} = \begin{bmatrix} -3.6 \cdot 10^{-1} & 0 & 5.9 \cdot 10^{-3} \\ 0 & -2.7 \cdot 10^{-1} & 0 \\ -2.5 \cdot 10^{-3} & 0 & -3.6 \cdot 10^{-2} \\ 0 & -1.0 \cdot 10^{-3} & 0 \\ -1.0 \cdot 10^{-3} & 0 & -9.1 \cdot 10^{-3} \\ 0 & 6.7 \cdot 10^{-2} & 0 \end{bmatrix} \qquad \begin{bmatrix} \frac{\partial F_{aero}}{\partial \omega} \\ \frac{\partial T_{aero}}{\partial \omega} \end{bmatrix} = \begin{bmatrix} 0 & -2.2 \cdot 10^{-3} & 0 \\ 2.2 \cdot 10^{-3} & 0 & 1.8 \cdot 10^{-1} \\ 0 & 9.3 \cdot 10^{-3} & 0 \\ -1.9 \cdot 10^{-2} & 0 & 2.5 \cdot 10^{-3} \\ 0 & 2.3 \cdot 10^{-2} & 0 \\ -2.2 \cdot 10^{-3} & 0 & -2.3 \cdot 10^{-1} \end{bmatrix}$$

Inertial damping:

$$\begin{bmatrix} \frac{\partial F_{inertia}}{\partial \omega} \\ \frac{\partial T_{inertia}}{\partial \omega} \end{bmatrix} = \begin{bmatrix} 0 & 1.71 \cdot 10^{-2} & 0 \\ -3.35 \cdot 10^{-2} & 0 & -3.16 \cdot 10^{-2} \\ 0 & -1.07 \cdot 10^{-2} & 0 \\ -6.11 \cdot 10^{-3} & 0 & 5.71 \cdot 10^{-3} \\ 0 & 1.26 \cdot 10^{-3} & 0 \\ -1.03 \cdot 10^{-2} & 0 & 4.85 \cdot 10^{-3} \end{bmatrix}$$

Left control FT:

$$\begin{bmatrix} \frac{\partial F}{\partial u_L} \\ \frac{\partial T}{\partial u_L} \end{bmatrix} = \begin{bmatrix} -0.14 & 0.26 & -0.31 & -0.24 & -0.54 & -0.27 & 0.19 & -0.55 & -0.06 & -0.03 & 0.23 & -0.34 \\ -0.10 & 0.33 & -0.02 & -0.16 & -0.15 & 0.04 & 0.50 & 0.14 & -0.15 & -0.16 & 0.47 & 0.15 \\ 0.18 & 0.82 & -0.29 & -0.18 & -0.38 & 0.26 & 1.23 & 0.06 & -0.03 & 0.08 & 1.24 & 0.19 \\ 0.07 & 0.43 & -0.24 & -0.13 & -0.25 & 0.10 & 0.53 & -0.04 & -0.03 & -0.00 & 0.55 & 0.11 \\ -0.03 & -0.10 & -0.02 & 0.06 & 0.06 & -0.03 & -0.06 & 0.04 & -0.01 & -0.04 & 0.11 & 0.16 \\ 0.05 & -0.33 & 0.23 & 0.20 & 0.38 & 0.14 & -0.10 & 0.18 & 0.11 & 0.12 & -0.06 & 0.18 \end{bmatrix}$$

Right control FT:

$$\begin{bmatrix} \frac{\partial F}{\partial u_R} \\ \frac{\partial T}{\partial u_R} \end{bmatrix} = \begin{bmatrix} -0.14 & 0.26 & -0.31 & -0.24 & -0.54 & -0.27 & 0.19 & -0.55 & -0.06 & -0.03 & 0.23 & -0.34 \\ 0.10 & -0.33 & 0.02 & 0.16 & 0.15 & -0.04 & -0.50 & -0.14 & 0.15 & 0.16 & -0.47 & -0.15 \\ 0.18 & 0.82 & -0.29 & -0.18 & -0.38 & 0.26 & 1.23 & 0.06 & -0.03 & 0.08 & 1.24 & 0.19 \\ -0.07 & -0.43 & 0.24 & 0.13 & 0.25 & -0.10 & -0.53 & 0.04 & 0.03 & 0.00 & -0.55 & -0.11 \\ -0.03 & -0.10 & -0.02 & 0.06 & 0.06 & -0.03 & -0.06 & 0.04 & -0.01 & -0.04 & 0.11 & 0.16 \\ -0.05 & 0.33 & -0.23 & -0.20 & -0.38 & -0.14 & 0.10 & -0.18 & -0.11 & -0.12 & 0.06 & -0.18 \end{bmatrix}$$

(Angular) velocity update:

$$\begin{bmatrix} v \\ \omega \end{bmatrix}_{i+1} = \begin{bmatrix} v \\ \omega \end{bmatrix}_i + A(x) + B(u_L, u_R)$$

Quaternion update:

$$q_{i+1} = \frac{1}{2} \begin{bmatrix} 2 & -\omega_x & -\omega_y & -\omega_z \\ \omega_x & 2 & \omega_z & -\omega_y \\ \omega_y & -\omega_z & 2 & \omega_x \\ \omega_z & \omega_y & -\omega_x & 2 \end{bmatrix}_{i+1} \cdot \begin{bmatrix} q_0 \\ q_x \\ q_y \\ q_z \end{bmatrix}_i$$

Quaternion normalization:

$$q_{i+1} = q_{i+1} / \|q_{i+1}\|$$

Position update:

$$p_{i+1} = p_i + \begin{bmatrix} 1 - 2(q_y^2 + q_z^2) & 2(q_x q_y - q_z q_0) & 2(q_x q_z + q_y q_0) \\ 2(q_x q_y + q_z q_0) & 1 - 2(q_x^2 + q_z^2) & 2(q_y q_z - q_x q_0) \\ 2(q_x q_z - q_y q_0) & 2(q_y q_z + q_x q_0) & 1 - 2(q_x^2 + q_y^2) \end{bmatrix}_{i+1} \cdot v_{i+1}$$

Extended Data Table 3| State-space parameters used for MPC-simulations. Note that all given parameters and values have been scaled using the scaling factors. Because the scaling makes the state-space parameters non-dimensional, the state update does not require a Δt as a time-step.

References

1. Grimaldi, D., Engel, M. S., Engel, M. S. & Engel, S. C. and P. M. S. *Evolution of the Insects*. (Cambridge University Press, 2005).
2. Deora, T., Gundiah, N. & Sane, S. P. Mechanics of the thorax in flies. *J. Exp. Biol.* **220**, 1382–1395 (2017).
3. Gu, J. *et al.* Recent advances in convolutional neural networks. *Pattern Recognition* **77**, 354–377 (2018).
4. Kramer, M. A. Nonlinear principal component analysis using autoassociative neural networks. *AIChE Journal* **37**, 233–243 (1991).
5. Pringle, J. W. S. The excitation and contraction of the flight muscles of insects. *J Physiol* **108**, 226–232 (1949).
6. Josephson, R. K., Malamud, J. G. & Stokes, D. R. Asynchronous muscle: a primer. *J. Exp. Biol.* **203**, 2713–2722 (2000).
7. Boettiger, E. G. & Furshpan, E. The mechanics of flight movements in diptera. *The Biological Bulletin* **102**, 200–211 (1952).
8. Pringle, J. W. S. *Insect Flight*. (Cambridge University Press, 1957).
9. Miyan J. A. & Ewing A. W. How Diptera move their wings: a re-examination of the wing base articulation and muscle systems concerned with flight. *Philosophical Transactions of the Royal Society of London. B, Biological Sciences* **311**, 271–302 (1985).
10. Wisser, A. Wing beat of Calliphora erythrocephala: Turning axis and gearbox of the wing base (Insecta, Diptera). *Zoomorphology* **107**, 359–369 (1988).
11. Ennos, R. A. A comparative study of the flight mechanism of diptera. *Journal of Experimental Biology* **127**, 355–372 (1987).
12. Dickinson, M. H. & Tu, M. S. The function of dipteran flight muscle. *Comparative Biochemistry and Physiology Part A: Physiology* **116**, 223–238 (1997).
13. Nalbach, G. The gear change mechanism of the blowfly (Calliphora erythrocephala) in tethered flight. *Journal of Comparative Physiology A* **165**, 321–331 (1989).
14. Walker, S. M., Thomas, A. L. R. & Taylor, G. K. Operation of the alula as an indicator of gear change in hoverflies. *Journal of The Royal Society Interface* **9**, 1194–1207 (2011).
15. Walker, S. M. *et al.* In Vivo Time-Resolved Microtomography Reveals the Mechanics of the Blowfly Flight Motor. *PLOS Biology* **12**, e1001823 (2014).
16. Wisser, A. & Nachtigall, W. Functional-morphological investigations on the flight muscles and their insertion points in the blowfly Calliphora erythrocephala (Insecta, Diptera). *Zoomorphology* **104**, 188–195 (1984).
17. Heide, G. Funktion der nicht-fibrillaren Flugmuskeln von Calliphora. I. Lage Insertionsstellen und Innervierungsmuster der Muskeln. *Zoologische Jahrbücher: Abteilung für Allgemeine Zoologie und Physiologie der Tiere* **76**, 87–98 (1971).
18. Fabian, B., Schneeberg, K. & Beutel, R. G. Comparative thoracic anatomy of the wild type and wingless (wg1cn1) mutant of Drosophila melanogaster (Diptera). *Arthropod Structure & Development* **45**, 611–636 (2016).

19. Tu, M. & Dickinson, M. Modulation of Negative Work Output from a Steering Muscle of the Blowfly Calliphora Vicina. *Journal of Experimental Biology* **192**, 207–224 (1994).

20. Tu, M. S. & Dickinson, M. H. The control of wing kinematics by two steering muscles of the blowfly (Calliphora vicina). *Journal of Comparative Physiology A* **178**, 813–830 (1996).

21. Muijres, F. T., Iwasaki, N. A., Elzinga, M. J., Melis, J. M. & Dickinson, M. H. Flies compensate for unilateral wing damage through modular adjustments of wing and body kinematics. *Interface Focus* **7**, 20160103 (2017).

22. O'Sullivan, A. *et al.* Multifunctional wing motor control of song and flight. *Current Biology* **28**, 2705-2717. e4 (2018).

23. Azevedo, A. *et al.* Tools for comprehensive reconstruction and analysis of Drosophila motor circuits. 2022.12.15.520299 Preprint at https://doi.org/10.1101/2022.12.15.520299 (2022).

24. Donovan, E. R. *et al.* Muscle Activation Patterns and Motor Anatomy of Anna's Hummingbirds Calypte anna and Zebra Finches Taeniopygia guttata. *Physiological and Biochemical Zoology* **86**, 27–46 (2013).

25. Lindsay, T., Sustar, A. & Dickinson, M. The function and organization of the motor system controlling flight maneuvers in flies. *Current Biology* **27**, 345–358 (2017).

26. Reiser, M. B. & Dickinson, M. H. A modular display system for insect behavioral neuroscience. *J. Neurosci. Meth.* **167**, 127–139 (2008).

27. Albawi, S., Mohammed, T. A. & Al-Zawi, S. Understanding of a convolutional neural network. in *2017 International Conference on Engineering and Technology (ICET)* 1–6 (2017). doi:10.1109/ICEngTechnol.2017.8308186.

28. Kennedy, J. & Eberhart, R. Particle swarm optimization. in *Proceedings of ICNN'95 - International Conference on Neural Networks* vol. 4 1942–1948 (1995).

29. Dana, H. *et al.* High-performance calcium sensors for imaging activity in neuronal populations and microcompartments. *Nature Methods* **16**, 649–657 (2019).

30. Fischler, M. A. & Bolles, R. C. Random sample consensus: a paradigm for model fitting with applications to image analysis and automated cartography. *Communications of the ACM* **24**, 381–395 (1981).

31. Heide, G. & Götz, K. G. Optomotor control of course and altitude in Drosophila melanogaster is correlated with distinct activities of at least three pairs of flight steering muscles. *Journal of Experimental Biology* **199**, 1711–1726 (1996).

32. Balint, C. N. & Dickinson, M. H. The correlation between wing kinematics and steering muscle activity in the blowfly Calliphora vicina. *Journal of Experimental Biology* **204**, 4213–4226 (2001).

33. Elzinga, M. J., Dickson, W. B. & Dickinson, M. H. The influence of sensory delay on the yaw dynamics of a flapping insect. *Journal of The Royal Society Interface* **9**, 1685–1696 (2012).

34. Dickinson, M. H., Lehmann, F.-O. & Sane, S. P. Wing rotation and the aerodynamic basis of insect flight. *Science* **284**, 1954–1960 (1999).

35. Lehmann, F. O. & Dickinson, M. H. The changes in power requirements and muscle efficiency during elevated force production in the fruit fly Drosophila melanogaster. *Journal of Experimental Biology* **200**, 1133–1143 (1997).

36. Lucia, S., Tătulea-Codrean, A., Schoppmeyer, C. & Engell, S. Rapid development of modular and sustainable nonlinear model predictive control solutions. *Control Engineering Practice* **60**, 51–62 (2017).

37. Cheng, B., Fry, S. N., Huang, Q. & Deng, X. Aerodynamic damping during rapid flight maneuvers in the fruit fly Drosophila. *Journal of Experimental Biology* **213**, 602–612 (2010).

38. Collett, T. S. & Land, M. F. Visual control of flight behaviour in the hoverfly, Syritta pipiens L. *J. Comp. Physiol.* **99**, 1–66 (1975).

39. Muijres, F. T., Elzinga, M. J., Iwasaki, N. A. & Dickinson, M. H. Body saccades of Drosophila consist of stereotyped banked turns. *J. Exp. Biol.* **218**, 864–875 (2015).

40. Muijres, F. T., Elzinga, M. J., Melis, J. M. & Dickinson, M. H. Flies evade looming targets by executing rapid visually directed banked turns. *Science* **344**, 172–177 (2014).

41. Snodgrass, R. E. *Principles of Insect Morphology*. (Cornell University Press, 2018).

42. Williams, C. M. & Williams, M. V. The flight muscles of Drosophila repleta. *Journal of Morphology* **72**, 589–599 (1943).

43. Wootton, R. The geometry and mechanics of insect wing deformations in flight: a modelling approach. *Insects* **11**, 446 (2020).

44. Takemura, S. *et al.* A Connectome of the Male Drosophila Ventral Nerve Cord. 2023.06.05.543757 Preprint at https://doi.org/10.1101/2023.06.05.543757 (2023).

45. Cheong, H. S. J. *et al.* Transforming descending input into behavior: The organization of premotor circuits in the Drosophila Male Adult Nerve Cord connectome. 2023.06.07.543976 Preprint at https://doi.org/10.1101/2023.06.07.543976 (2023).

46. Martynov, A. B. Über zwei Grundtypen der Flügel bei den Insecten und ihre Evolution. *Zeitschrift für Morphologie und Ökologie der Tiere* **4**, 465–501 (1925).

47. Wipfler, B. *et al.* Evolutionary history of Polyneoptera and its implications for our understanding of early winged insects. *Proceedings of the National Academy of Sciences* **116**, 3024–3029 (2019).

48. Hasenfuss, I. The evolutionary pathway to insect flight – a tentative reconstruction. *Arthropod Systematics and Phylogeny* **66**, 19–35 (2008).

49. Willkommen, J. & Hörnschemeyer, T. The homology of wing base sclerites and flight muscles in Ephemeroptera and Neoptera and the morphology of the pterothorax of Habroleptoides confusa (Insecta: Ephemeroptera: Leptophlebiidae). *Arthropod Structure & Development* **36**, 253–269 (2007).

50. Willmann, R. Advances and problems in insect phylogeny. in *Arthropod Relationships* (eds. Fortey, R. A. & Thomas, R. H.) 269–279 (Springer Netherlands, 1998). doi:10.1007/978-94-011-4904-4_20.

51. Kwon, Y.-H. DLT Method. http://www.kwon3d.com/theory/dlt/dlt.html.

52. Götz, K. G. Course-Control, Metabolism and Wing Interference During Ultralong Tethered Flight in Drosophila Melanogaster. *Journal of Experimental Biology* **128**, 35–46 (1987).

53. Klambauer, G., Unterthiner, T., Mayr, A. & Hochreiter, S. Self-Normalizing Neural Networks. in *Advances in Neural Information Processing Systems* vol. 30 (Curran Associates, Inc., 2017).

54. Grewal, M. S. & Andrews, A. P. *Kalman Filtering: Theory and Practice with MATLAB*. (John Wiley & Sons, 2014).

55. Dykstra, R. L. An algorithm for restricted least squares regression. *Journal of the American Statistical Association* **78**, 837–842 (1983).

56. Runge, C. Über empirische Funktionen und die Interpolation zwischen äquidistanten Ordinaten. *Zeitschrift für Mathematik und Physik* **46**, 224–243 (1901).

57. Birch, J. M. & Dickinson, M. H. The influence of wing–wake interactions on the production of aerodynamic forces in flapping flight. *Journal of experimental biology* **206**, 2257–2272 (2003).

58. Dickinson, M. H. & Götz, K. G. The Wake Dynamics and Flight Forces of the Fruit Fly Drosophila Melanogaster. *Journal of Experimental Biology* **199**, 2085–2104 (1996).

59. Cheng, B. & Deng, X. Translational and rotational damping of flapping flight and its dynamics and stability at hovering. *IEEE Transactions on Robotics* **27**, 849–864 (2011).

60. van Veen, W. G., van Leeuwen, J. L. & Muijres, F. T. A chordwise offset of the wing-pitch axis enhances rotational aerodynamic forces on insect wings: a numerical study. *Journal of The Royal Society Interface* **16**, 20190118 (2019).

61. Dickson, W. B., Polidoro, P., Tanner, M. M. & Dickinson, M. H. A linear systems analysis of the yaw dynamics of a dynamically scaled insect model. *Journal of Experimental Biology* **213**, 3047–3061 (2010).

62. Kouvaritakis, B., C., M. *Model Predictive Control*. (Springer International, 2016).

63. Lerch, S. *et al.* Resilin matrix distribution, variability and function in Drosophila. *BMC Biology* **18**, 195 (2020).